Universidade Federal do Piauí
Centro de Ciências da Natureza
Programa de Pós-Graduação em Física

Mestrado em Física

Transporte eletrônico em nanojunções triangulares de carbono com três terminais

—

Electronic transport in three-terminal triangular carbon nanopatches

Ana Luiza Mariano Torres Costa

Dissertação de Mestrado

Orientador:
Prof. Dr. Eduardo Costa Girão

Teresina – PI
Janeiro/2015

Universidade Federal do Piauí
Centro de Ciências da Natureza
Programa de Pós-Graduação em Física

Mestrado em Física

Ana Luiza Mariano Torres Costa

Transporte eletrônico em nanojunções triangulares de carbono com três terminais

—

Electronic transport in three-terminal triangular carbon nanopatches

Dissertação apresentada ao Programa de Pós-Graduação em Física da Universidade Federal do Piauí como parte dos requisitos para a obtenção do título de Mestre em Física.

Orientador:
Prof. Dr. Eduardo Costa Girão

Teresina – PI

Janeiro/2015

Universidade Federal do Piauí
Centro de Ciências da Natureza
Programa de Pós-Graduação em Física
Mestrado em Física

Ana Luiza Mariano Torres Costa

Transporte eletrônico em nanojunções triangulares de carbono com três terminais

—

Electronic transport in three-terminal triangular carbon nanopatches

Dissertação apresentada ao Programa de Pós-Graduação em Física da Universidade Federal do Piauí como parte dos requisitos para a obtenção do título de Mestre em Física.

Prof. Dr. Eduardo Costa Girão
Universidade Federal do Piauí
Orientador

Prof. Dr. José Pimentel de Lima
Universidade Federal do Piauí

Prof. Dra. Aldilene Saraiva Souza
Universidade Federal do Ceará

Prof. Dr. Acrísio Lins de Aguiar
Universidade Federal do Piauí

Aprovada em Janeiro/2015.

À minha família.

Acknowledgments

I thank to my parents for all the support, that they provided me all my life time.

I thank to my advisor, for his time and patience.

I thank to my colleagues for useful technical discussions.

I thank to the Universidade Federal do Piauí, for my formation opportunities.

I thank to Coordenação de Aperfeiçoamento de Pessoal de Nível Superior (CAPES) for financial support.

Resumo

Nesta dissertação, as propriedades de transporte eletrônico de junções grafíticas de três terminais são estudadas utilizando-se uma combinação de método *tight-binding* e teoria de transporte eletrônico baseada nos formalismos de funções de Green e de Landauer. As junções são compostas de uma estrutura triangular composta de três nanofitas de grafeno de borda *armchair* unidas de modo a formar um triângulo equilátero. Nós mostramos como detalhes da região central influenciam o transporte ressonante através das regiões triangulares e destacamos as características especiais do fluxo de corrente como função da geometria. Estas propriedades explicitam um conjunto de funcionalidades visando o desenvolvimento de nanocircuitos complexos baseados no carbono e de dispositivos operacionais em nanoescala.

Palavras-Chave: Nanofita de grafeno, função de Green, transporte eletrônico.

Abstract

The electronic transport properties of three-terminal graphene-based triangular patches are investigated using a combination of semi-empirical tight-binding calculations and Green's function-based transport theory within Landauer's framework. The junctions are composed of a triangular structure based on armchair edged graphene nanoribbons. We show how details of the central region influence the resonant electronic transport across the triangular patches and highlight the unique features of the current flow as a function of geometry. These properties indicate an array of functionalities for the development of carbon-based complex nanocircuits and operational devices at the nanoscale.

Keywords: Graphene nanoribbons, green's functions, electronic transport.

"Imagination is more important than knowledge. For knowledge is limited to all we now know and understand, while imagination embraces the entire world, and all there ever will be to know and understand.."

– Albert Einstein –

Contents

List of Figures

1 The Nano World

"Nano" is a prefix which is appeariang more frequently in science, technology and even in the media. The size of electronic devices is decreasing in size and we can see this miniaturization. Before, most electronic components could be easily seen as they have the size of some centimeters, as the valves of the first computers. With the passing of decades, these objects were miniaturized and started having dimensions of millimeters, in other words, they had a ten times reduction in their size and these dimensions were decreasing to micrometers until we reach the nanoscale. This Chapter is dedicated to talk about nanoscience and nanotecnology. We will discuss historical aspects, the evolution over the years and the impacts in the society.

1.1 The beginnings of Nanoscience

Nano is the prefix for units of 10^{-9}, so that one nanometer is a billionth part of a meter or a millionth of a millimeter. In 1959, Richard Feynman envisioned nanotechnology for the first time in his lecture "Plenty of room at the bottom", at the (look for the conference name). He questioned if it was possible for us to write the entire 24 volumes of the Encyclopedia Brittanica on the head of a pin. Feynman imagined the future and challenged the audiences saying: "It's my intention to offer a prize of 1,000 dollars to the first guy who can take the information on the page of book and put it on an area 1/25,000 smaller in linear scale in such manner that it can be read by an electron microscope. And I want to offer another 1,000 dollars to the first guy who makes an operating electric motor, a rotating motor which can be controlled from the outside and, not counting the lead-in wires, is only 1/64 inch cube" [3]. In Feynman' opinion, there was so much space in the small scale that if we could manipulate atoms individually, then we could create things as small as we wanted. We know, since a long time ago, that everything on Earth is made up of atoms and now the science is learning to do different things from atoms. This is the essential concept for nanoscience, proposed by Feynman decades ago. Nanotechnology is already present in some applications in different areas, like medicine, chemistry, biology, physics and materials science, and consists in the ability

of seeing and controlling individual atoms and molecules below 100 nanometres in one or more dimensions. However, this is a new and hard world to explore, since matter presents new properties at the nanoscale. For this reason, a large effort on research has been devoted to the aim of building knowledge which can enable the development of new technologies based on the properties of materials when manipulated at the nanoscale. As a result, possible nanotechnology applications can be seen in medicine, for example, where nanomaterials allow the development of good implants. In addition, there is a potential market for nanoparticles to be used as vehicles for drugs delivery and in cosmetics. Nanotechnology can also act in environmental applications since nanoparticles have the hability to adsorve selected contaminants from water, for instance [4]. Another practical nanomaterial application, was presented by Tans and *co-workers*, where they fabricated a nanotransistor based in a single walled carbon nanotube, in the latter nineties [5]. An application still more surprising and recent may be found in the carbon nanotube based computer, presented by Shulaker *et al* [6], and these are only two drops in the vast sea of nanotech applications. In the nanotechnology scenery, carbon is certainly one of the most important elements. Since the antiquity it is used in some applications and more and more scientific studies involving this element have been done. This is because this element combine easily to form a big variety of nanostructures that may be used for many applications. We will talk about this element in next section and explain why carbon is so scientifically and technologically important.

1.2 The Carbon

Back to the beginning of the planet, carbon was present with hidrogen, nitrogen and oxigen creating essential conditions to the appearance of life on earth, so the carbon is the essential element around which developed life. But why the carbon is chosen to be this element? Why not one of the others elements? This is because its atomic structure which allows for the formation of a larger variety of structures compared to many others elements. Carbon is the sixth element of the periodic table of elements, having four electrons in its valence. The most important characteristic of carbon is its versatile ability to share electrons with another carbon atoms so as to form different configurations of carbon-carbon bonds, this is the basis of organic chemistry. Silicon, like carbon can form these bonds, but at the earth atmosphere the compounds based on silicon-silicon bonds oxidize forming silica, which makes sand and quartz. These materials do not provide life on earth. Because this, carbon is the spinal cord of organic chemistry and the molecular components of living things.

Carbon also forms inorganic structures. Diamond and graphite, are the "old allotropes" of carbon. In the diamond structure, each carbon atom bonds to four other carbon atoms in a tetrahedral geometry. This is the most resistant material in nature. The graphite consist of the superposition of layers called graphene sheets. The carbon atom has strong covalent bonds inside the layer and bonds to three another carbon atoms through covalent bonds of the σ type. The fourth electron of each carbon atom forms a itinerant bond of the type π, what makes the graphite a good conductor. Exist a weaker attraction between the layers of graphite and them can be easily separated. The atomic structures for diamond and graphite could be seen in Figure 1.1.

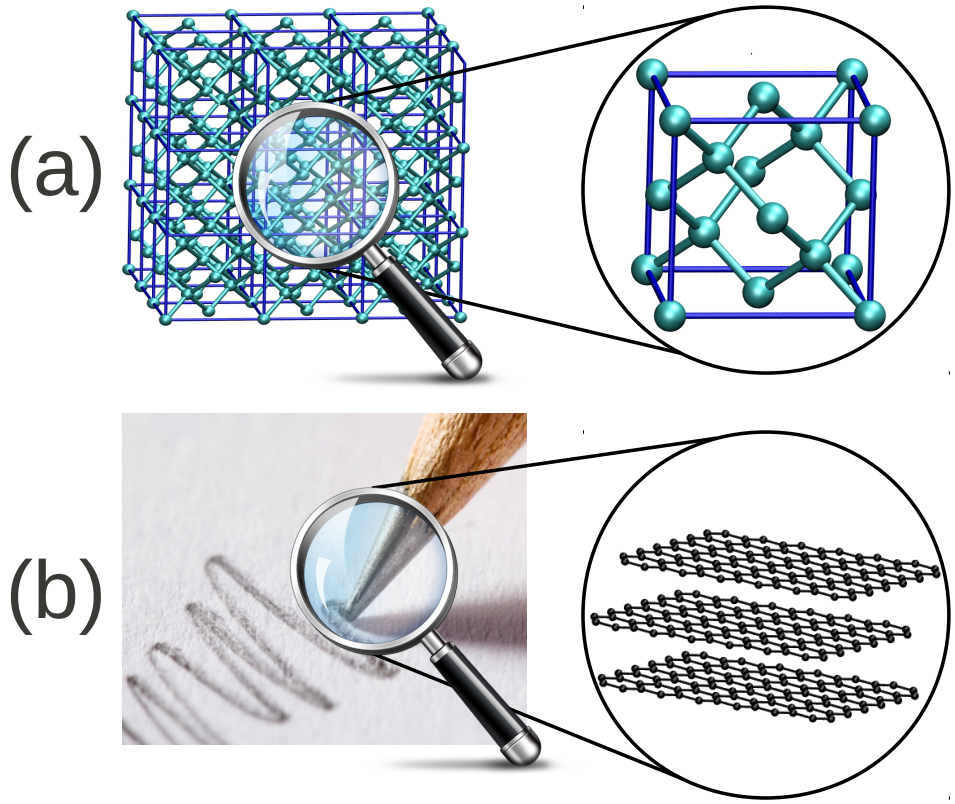

Figure 1.1: Illustration of the diamond (a) and graphite (b) structures.

1.3 Hybridization

Carbon atoms has six electrons that obey, in ground state, the following configuration $1s^2 2s^2 2p^2$. The $1s^2$ orbital contains two electrons strongly bounded to the nucleus and they are called core electrons. Four electrons occupy the $2s^2 2p^2$ orbitals, and these more weakly bounded electrons are called valence electrons.

Once the energy step between the upper $2p$ energy levels and the lower $2s$ level for carbon is not very high compared with the binding energy of the chemical bonds [7], the

electrons of these orbitals can easily assume states that are linear combination of $|2s\rangle$, $|2p_x\rangle$, $|2p_y\rangle$ and $|2p_z\rangle$. These combinations are called sp^n hibridization, where n depends of the number and directions of the bonds. We have three main hybridization schemes which involve one $2s$ orbital and one (sp), two (sp^2) or three (sp^3) $2p$ orbitals.

1.3.1 *sp* hybridization

The s orbital mix with one of the p orbital (p_x, for example) to form this hybridization. The two orbitals hybridized denoted by $|sp_a\rangle$ and $|sp_b\rangle$ are expressed by linear combination of original orbital [7],

$$\begin{aligned} |sp_a\rangle &= \frac{1}{\sqrt{2}}(|2s\rangle + |2p_x\rangle), \\ |sp_b\rangle &= \frac{1}{\sqrt{2}}(|2s\rangle - |2p_x\rangle), \end{aligned} \tag{1.1}$$

This hybridization occurs when the atoms form linear chains, like in polyyne chains. A simple carbon-based material showing this hybridization is acetylene. The schematic representations of these hybrid orbitals are shown in Figure 1.2a.

1.3.2 sp^2 hybridization

The sp^2 hybridization, is characterized by the merge of, one s orbital and two p orbitals (p_x e p_y, for instance) thus hybridized to produce hybrid orbitals allowing the formation of three identical bonds making a 120° angle with each other. We will call these orbitals sp_a^2, sp_b^2 and sp_c^2. To get them we are going to use *2p* orbitals pointing in the following directions: $(0,-1,0)$, $(\frac{\sqrt{3}}{2},\frac{1}{2},0)$ e $(-\frac{\sqrt{3}}{2},\frac{1}{2},0)$, respectively. Due the symmetry of the *2s* orbital your coefficient for each orbital must be the same. This way, we can write:

$$\begin{aligned} |sp_a^2\rangle &= C|2s\rangle - \sqrt{1-C^2}[-|2p_y\rangle], \\ |sp_b^2\rangle &= C|2s\rangle + \sqrt{1-C^2}[\frac{\sqrt{3}}{2}|2p_x\rangle + \frac{1}{2}|2p_y\rangle], \\ |sp_c^2\rangle &= C|2s\rangle + \sqrt{1-C^2}[-\frac{\sqrt{3}}{2}|2p_x\rangle + \frac{1}{2}|2p_y\rangle], \end{aligned} \tag{1.2}$$

and using orthonormality conditions of $|sp_a^2\rangle$ and $|sp_b^2\rangle$, we can determine the coefficient C

$$C^2 - \frac{1}{2}(1-C^2) = 0 \Rightarrow C = \pm\frac{1}{\sqrt{3}}. \tag{1.3}$$

A suggestive example for this hybridization is the graphene sheet. The schematic representations of these hybrid orbitals are shown in Figure 1.2b.

1.3.3 sp^3 hybridization

This hybridization involves the s orbital and all three p orbitals. The carbon atom makes four identical bonds, creating a tetrahedron. The four directions of tetrahedral bonds from the carbon atom can be selected as $(1,1,1)$, $(-1,-1,1)$, $(-1,1,-1)$ and $(1,-1,1)$ [7], forming four hybridic orbitals which will be called sp_a^3, sp_b^3, sp_c^3 and sp_d^3. The linear combinations are

$$\begin{aligned}
|sp_a^3\rangle &= C|2s\rangle + \sqrt{1-C^2}\frac{1}{\sqrt{3}}[|2p_x\rangle + |2p_y\rangle + |2p_z\rangle],\\
|sp_b^3\rangle &= C|2s\rangle + \sqrt{1-C^2}\frac{1}{\sqrt{3}}[-|2p_x\rangle - |2p_y\rangle + |2p_z\rangle],\\
|sp_c^3\rangle &= C|2s\rangle + \sqrt{1-C^2}\frac{1}{\sqrt{3}}[-|2p_x\rangle + |2p_y\rangle - |2p_z\rangle],\\
|sp_c^3\rangle &= C|2s\rangle + \sqrt{1-C^2}\frac{1}{\sqrt{3}}[-|2p_x\rangle - |2p_y\rangle + |2p_z\rangle],
\end{aligned} \tag{1.4}$$

and using orthonormality conditions

$$C^2 - \frac{1}{3}(1-C^2) = 0 \Rightarrow C = \frac{1}{2}. \tag{1.5}$$

Such hybridization is found in methane (CH_4) and in diamond. The schematic representations of these hybrid orbitals are shown in Figure 1.2c.

1.4 Carbon-based nanostructures

New carbon allotropes were discovered starting in the 80's. In 1985, Kroto, Curl and Smalley [8] discovered the fullerenes, a spherical molecule made of 60 carbon atoms, and were awarded the Nobel Prize in chemistry in 1996. We can see this atomic structure in Figure 1.3a. The interest and attention to carbon start to grow and, in 1991, S. Iijima published a paper which reported the existence of carbon nanotubes [9]. That form was the multi-wall carbon nanotubes (MWNT). Two years later, the single-wall carbon nanotubes are discovered by Iijima [10] and Bethune [11]. A carbon nanotube structure is illustrated in Figure 1.3b.

Although graphene was known since a long time, the scientists succeeded in isolating just a single layer structure only in 2004 [12]. The resulting structure is a 2D material composed of carbon atoms, having a thickness of only one atom and it is called graphene. Graphene have interesting physical and chemical properties and it is a prospective material for nanotechnology. We can see its atomic structure in Figure 1.3c. In the following, we

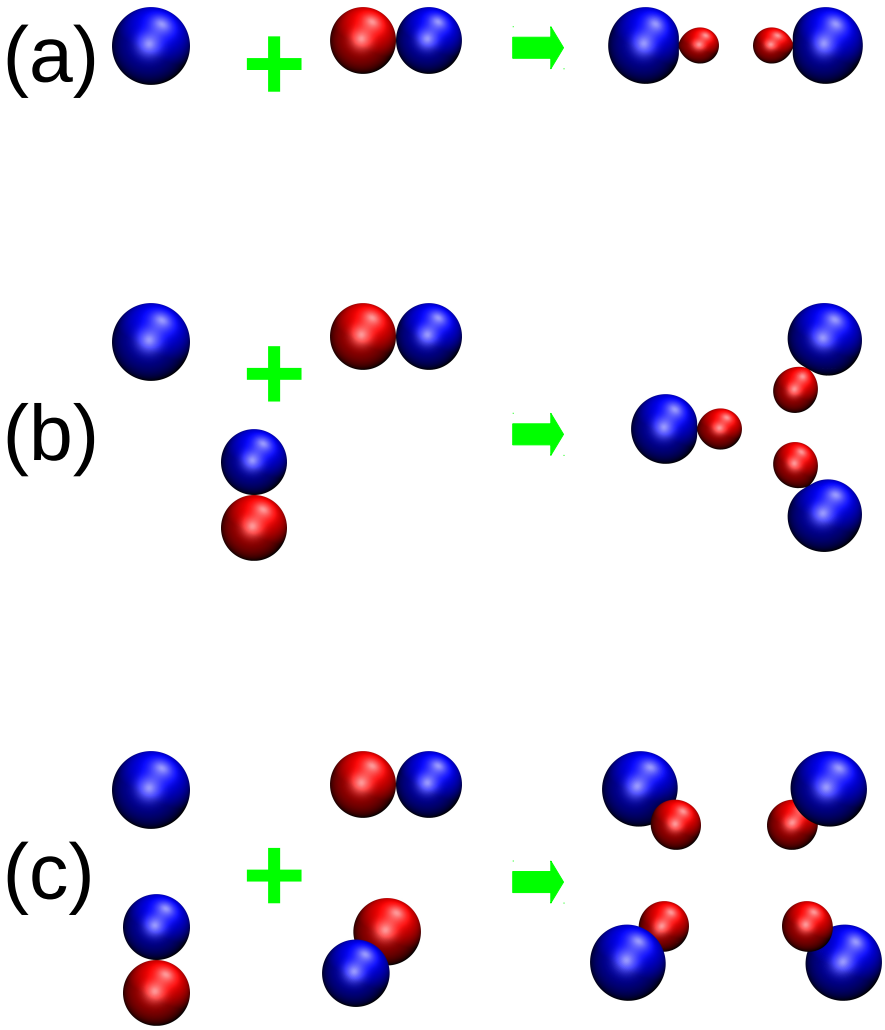

Figure 1.2: sp (a) sp^2 (b) and sp^3 hybridizations.

discuss about these carbon nanostructures.

1.5 Fullerenes and Carbon Nanotubes

In the fullerene structure, the carbon atoms are arranged on a spherical surface (C_{60}) or oval surface (C_{70}). The first are also called buckyballs, since the carbon atoms are placed in such way that they remember the seam of an old soccer ball. These structures are composed by hexagons and pentagons (the last one are responsible for the curvature). Carbon has an intermediary hybridization between sp^2 and sp^3.

The nanotube structure can be viewed as a graphene sheet rolled up into a tube. Depending on the way how to roll the sheet, we have an armchair, zigzag or chiral nanotube [7]. The studies involving nanotubes excited the scientific community, because they have special properties. They show a unique combination of stiffness, strength, and tenacity compared to other fiber materials which usually lack one or more of these prop-

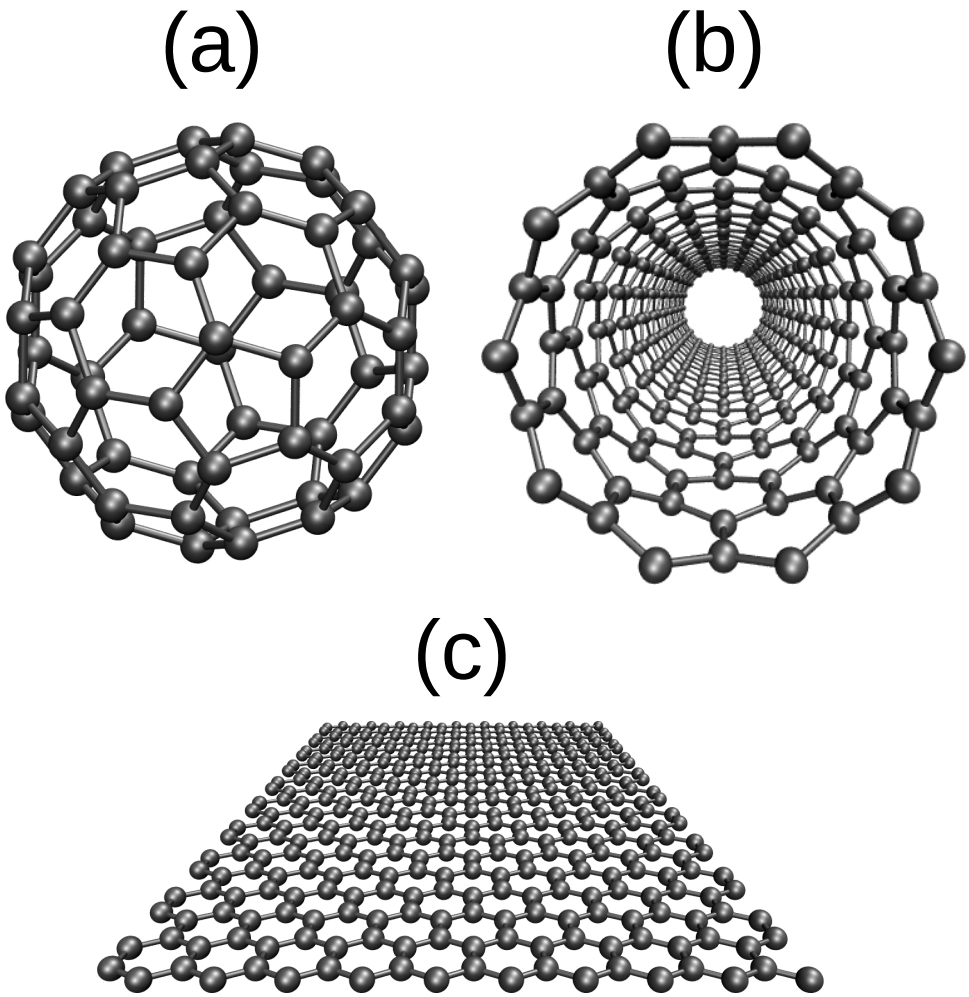

Figure 1.3: Fullerene (a) nanotube (b) and graphene (c).

erties. Thermal and electrical conductivity are also very high, and comparable to other conductive materials.

The researches involving nanotubes made great progress in the laboratory. In 1998, physicists demonstrate a transistor made from a single, semiconducting nanotube. In 2007, researchers reported the synthesis of a carbon nanotube based transistor radio. The applications using nanotubes that were most successful is in composite materials for planes and automobiles. Besides the commercialization of nanotube based conducting films for energy storage and touch screens is very close to become a fact, according to the Ref. [13]. But some difficulties remain to the use of nanotubes in electronics, because of contact resistance.

1.6 Graphene

After its isolation, graphene has been the focus of intense scientific investigations both in theory and experiments, making graphene a hot subject in materials science. In 2010, graphene was the subject of around 3000 research papers and more than 400 patent applications [13]. The effective mass of electrons in graphene tends to zero. Because this they have a high electronic mobility (hundred times larger than silicon that is very used in nanoelectronics). This explains its high thermal conductivity and the good electrical conductivity, making graphene a promising material to be used in electronics. Furthermore, graphene has some advantages in comparison to carbon nanotubes or fullerenes regarding the control in their synthesis. But graphene is not perfect, it has problems too. We will talk about this in next section, where we will study its electronic structure. Looking into graphite's case, the graphene's layers are held together, due to van der Walls forces, which makes such interaction between two adjacent layers very small compared to the intra-layer bonds, which are very well known to be covalent bonds. The graphene's atomic structure, shown in Fig. 1.4, can be described as a Bravais lattice with a basis composed by two atoms, or two identical inter-penetrating lattices. Considering the system in xy plane, $\mathbf{a}_1$ and $\mathbf{a}_2$ are unit vectors in real space of the hexagonal lattice and are expressed as

$$\mathbf{a}_1 = (\frac{\sqrt{3}}{2}a, \frac{a}{2}), \qquad \mathbf{a}_2 = (\frac{\sqrt{3}}{2}a, -\frac{a}{2}), \tag{1.6}$$

with $a = a_{cc}\sqrt{3}$. In the reciprocal space, we have the vectors $\mathbf{b}_1$ and $\mathbf{b}_2$, that are given by:

$$\mathbf{b}_1 = (\frac{2\pi}{\sqrt{3}a}, \frac{2\pi}{a}), \qquad \mathbf{b}_2 = (\frac{2\pi}{\sqrt{3}a}, -\frac{2\pi}{a}). \tag{1.7}$$

We know that the limits of miniaturization of the electronics based on silicon are approaching their limit, and graphene is regarded as a potential candidate to replace silicon technology [13] and some companies already consider this material as one of the technologies of the future. Even though there is a lot of work to do until these nanostructures based in carbon transform in technology to be available in stores, a huge effort in research is being developed by the scientific community and many important results were already obtained in the quest for to reduce the waiting time for the use of the graphene in commercial scale.

1.6.1 Graphene's electronic structure

The band structure of the material is a fundamental information when we study a nanoscale systems. This is because it gives us the allowed values of energy to the electrons

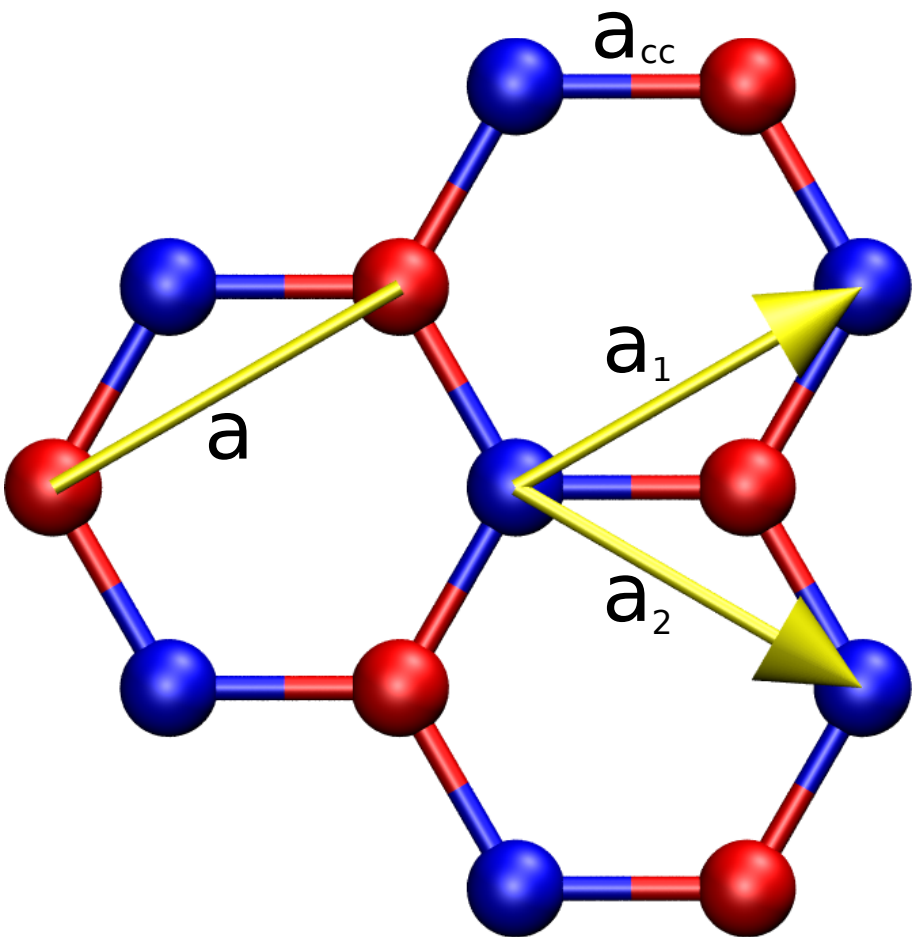

Figure 1.4: Graphene bands structure with the honeycomb vectors.

of the system. In graphene, we can calculate the electronic structure using a tight-binding model that will be explained better in chapter 2. According to this method, we can write

$$E_{g2D}(k_x, k_y) = \pm\gamma\left[1 + 4\cos\left(\frac{\sqrt{3}k_x a}{2}\right)\cos\left(\frac{k_y a}{2}\right) + 4\cos^2\left(\frac{k_y a}{2}\right)\right]^{\frac{1}{2}}, \tag{1.8}$$

where (k_x, k_y) is the wave vector and γ is the first neighbor hopping interaction. In Fig. 1.5 we plot this relation at the first Brillouin zone on the axes of high symmetry ΓM, ΓK e MK. The density of states at the Fermi level is zero, so the graphene is a semiconductor with zero gap.

1.6.2 Graphene nanoribbons

Graphene is a very interesting material and it is accepted as a potential candidate for replacing silicon in the future technology. This material has a rich physics and because this it has gained a rapid growth in the number of scientific publications based on both experimental and theoretical studies.

Graphene is a very good conductor. Its ideal infinite structure do not have an energy

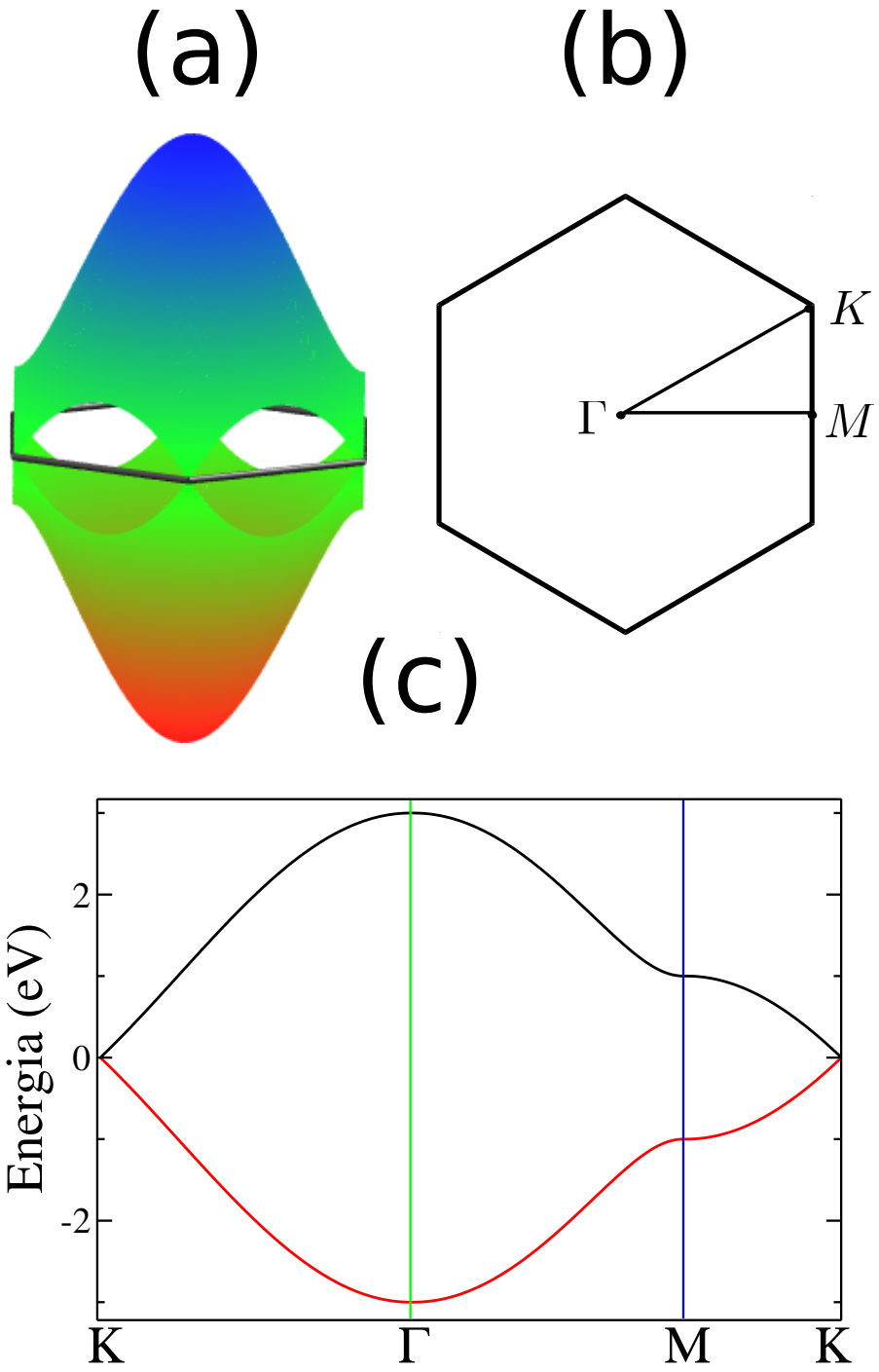

Figure 1.5: Eletronic band structure for the graphene shown over the Brillouin zone and along the high symmetry lines.

gap and this is a problem because the presence of an energy gap is fundamental for some applications in nanoelectronics. To this end, the scientists started to study many possibilities to modify graphene's structure creating an opening of the energy bands around the Fermi level. Many methods show themselves to be capable to do it, like molecular doping, defects, among others. One possibility for opening a band gap in graphene based systems, is cutting down the entire graphene layer into very narrow stripes, thus creating

structures called graphene nanoribbons (GNRs), which are quasi -unidimensional systems, then confining the electron in one direction. [14, 2, 15]. Due to the confinement in one direction, the electronic structure is quite dependent on their width and edge. They can be either a semiconductor or a metal [14, 16]. These properties open many possibilities for applications of the GNRs in electronic nanodevices. The main geometries for GNRs are armchair (A-GNR, Fig. 1.6a) and zigzag (Z-GNR, Fig. 1.6b).

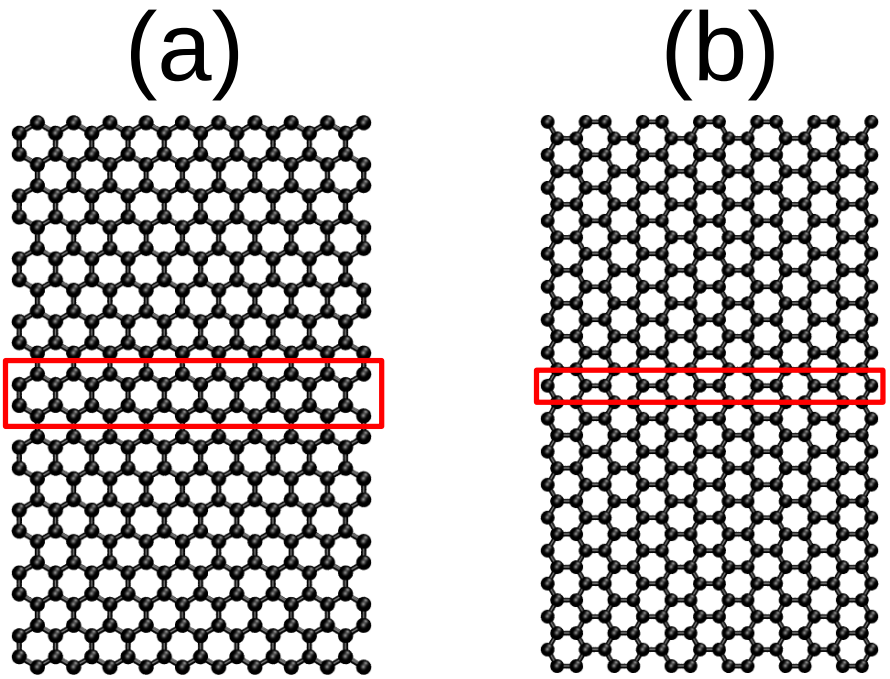

Figure 1.6: Armchair graphene nanoribbon A-GNR (a) and zig-zag graphene nanoribbon Z-GNR (b). The red boxes indicate the GNRs unit cells.

A-GNRs are semiconductors and their energy gap Δ_n is strongly dependent on its width, as we can see in the graph of Fig. 1.7. The gap decreases as we increase the ribbon width. Here we show the bands structure for three A-GNRs with 8, 9 e 10 $C-C$ lines respectively. ,These were calculated using the Tight-Binding method described in Chapter 2. The width of the A-GNR is denoted for the number of $C-C$ (N_{CC}) lines along the periodic direction of the ribbon ($N_{CC}=20$ in Fig. 1.6a). The distance between two $C-C$ lines is $a_{CC}\frac{\sqrt{3}}{2}$, the width W_a of an A-GNR (without considering the hydrogens on the edges), may be obtained by:

$$W_a = \frac{(N-1)a_{CC}\sqrt{3}}{2}. \tag{1.9}$$

Depending the width, the Δ_n *versus* N_{CC} curve has three different branches so that $\Delta_{3n+1} \geq \Delta_{3n} \geq \Delta_{3n-1}$ [14], as shown in Figure 1.8. In all cases, the gap tends to zero,

when $N_{CC} \to \infty$.

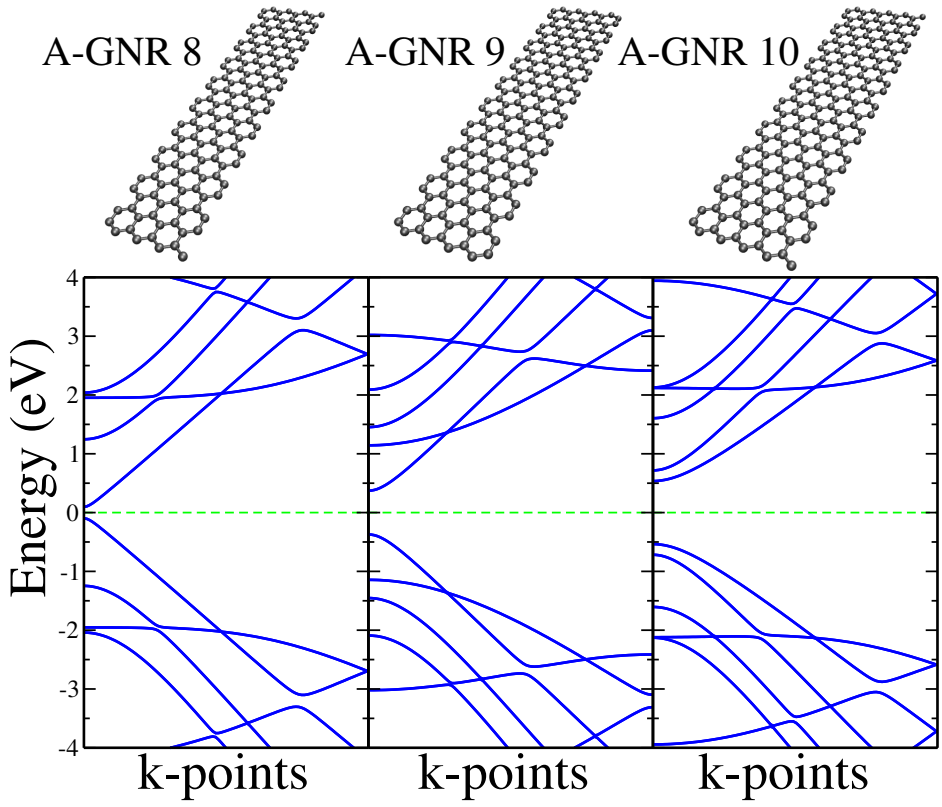

Figure 1.7: Bands structures for A-GNRs with 8, 9 and 10 $C-C$ lines. The green line corresponds a Fermi Level.

The Z-GNRs have a more interesting set of properties than A-GNRs. This particular edge geometry has a ferromagnetic spin polarization, absent in A-GNRs. The edge-to-edge polarization can be of two distinct configurations, ferromagnetic (FM) where the spin moments on both edges point in the same direction or antiferromagnetic (AFM) where the spins are anti-parallel edge-to-edge [16], where the latter one is the ground state. There is another configuration, that we called paramagnetic (PM), where the edges of Z-GNRs are non-polarized. We illustrated these cases with their correspondent band structure, obtained using the TBU method (Chapter 2), with the parameterization proposed by [17], in Fig. 1.9.

The length of a unit cell, in a Z-GNR is $a_{CC}\sqrt{3}$ and the width W_Z (without considering the hydrogens on the edges), can be obtained by:

$$W_Z = \frac{(3N-2)a_{cc}}{2} \tag{1.10}$$

where N_{ZZ} is the number of $Z-Z$ lines along the periodic direction of the ribbon ($N_{ZZ} =$ 12 in Fig. 1.6b).

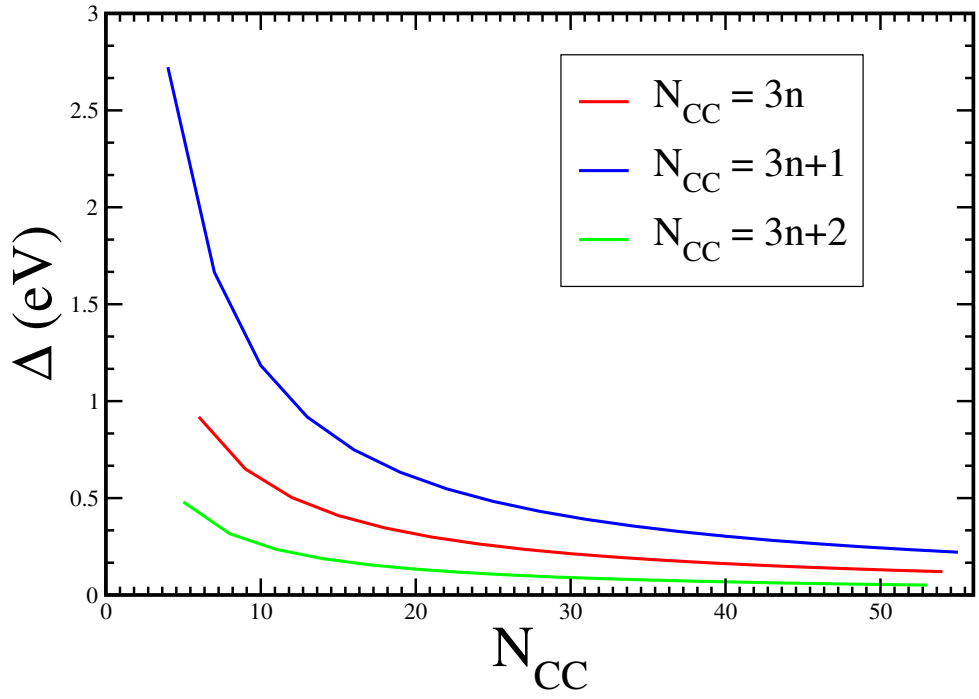

Figure 1.8: Three families of gaps for an A-GNR (Δ) as a function of the number of $C-C$ lines (N_{CC}).

The PM and FM states are metallic, while the AFM is a semiconductor since their bands do not touch the Fermi level. We can also observe that in the AFM case the spin up and spin down polarizations edge-to-edge belong to different graphene sub-lattices, that makes the AFM to be the ground state. These magnetic configurations for Z-GNRs have called much attention for future applications in nanoelectronics and spintronics. Another caracterist for Z-GNRs is that the magnetic properties can be controlled for an external electric field, this is proposed by Son *et. al.* [18], where they predicted that if in-plane homogeneous electric fields are applied across the zigzag-shaped edges of the graphene nanoribbons, a half-metallic behavior is induced which refers to the coexistence of a metallic state for electrons with a spin orientation and an insulating state for electrons with opposite spin orientation.

1.7 Fabrication of nanostructures

Until now we discuss about some interesting theoretical properties, but is very important to have an experiential view to verify the validity of the theory. Is it possible to reproduce this structures experimentally? Several studies have shown that it is possible and different approaches have been proposed to obtain GNRs. These efforts can be classify in two groups: bottom-up [2] and top-down [19].

The bottom-up approach is based on the self-assembly phenomenon. The main idea of

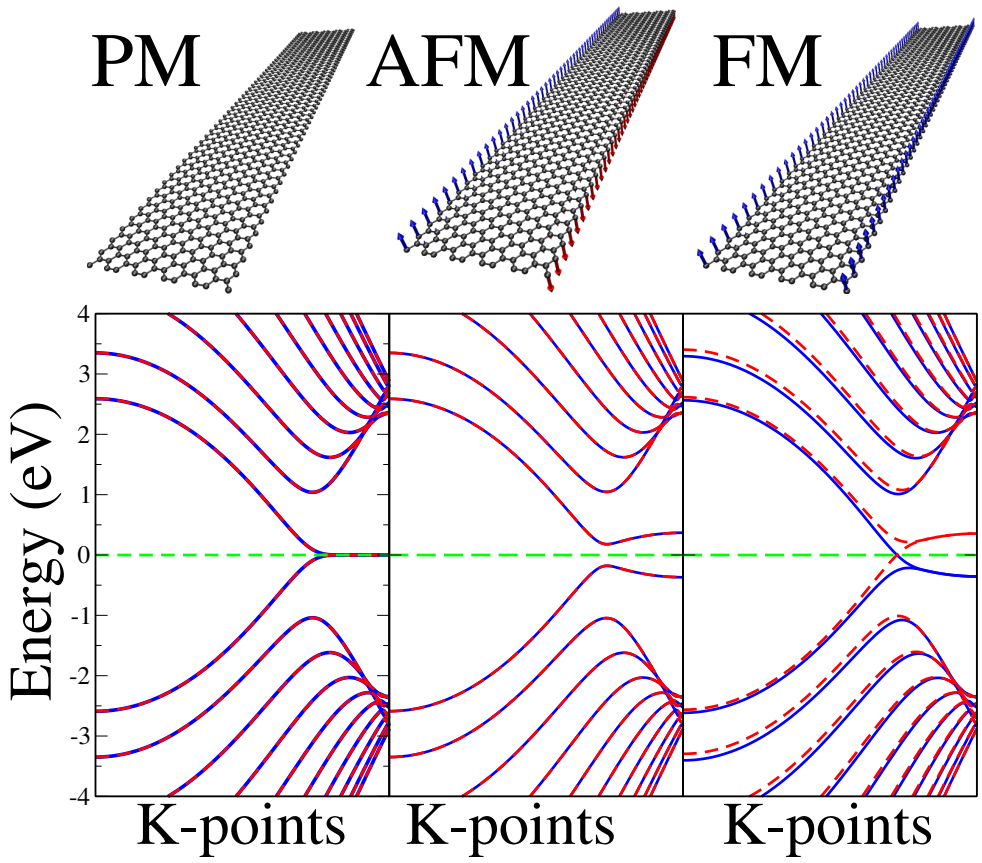

Figure 1.9: Paramagnetic (PM), anti-ferromagnetic (AFM) and ferromagnetic (FM) states and their correspondent bands structure. The dashed green line is the Fermi level, the blue line correspond spin up, and the dashed red line correspond spin down.

this strategy is the development of the self-assembly of the atoms, molecules and molecular chains into nanoscale objects. In the other words, it is the process of formation of complex ordered structures from simpler ones. The bottom-up approach is opposite in principle to the top-down approach, which is based on the sequential decrease of the object size by means of mechanical or chemical processing for the fabrication of nano-objects [20].

There are many techniques of fabrication of nanostructures. We can cite some examples of experimental techniques to create GRNs. Kosynkin *et. al* [1] reported the fabrication of GNRs using a longitudinal unzipping of carbon nanotubes, that consists by suspending MWCNTs (multi-walled carbon nanotubes) in concentrated sulphuric acid followed by treatment of $KMnO_4$ at room temperature and then heating them at $55-70°C$. It is known that, after isolation process, the outcoming nanoribbons were found highly soluble in solvents like water, ethanol and other polar organic solvents. They used SWCNTs (single-walled carbon nanotubes), to produce narrow nanoribbons, but their subsequent disentanglement is more difficult. This method is illustrated in Fig. 1.10.

A bottom-up approach, proposed by Cai and co-workers [2], has shown to be extremely effective to produce GNRs with atomic scale precision. They were able to produce two

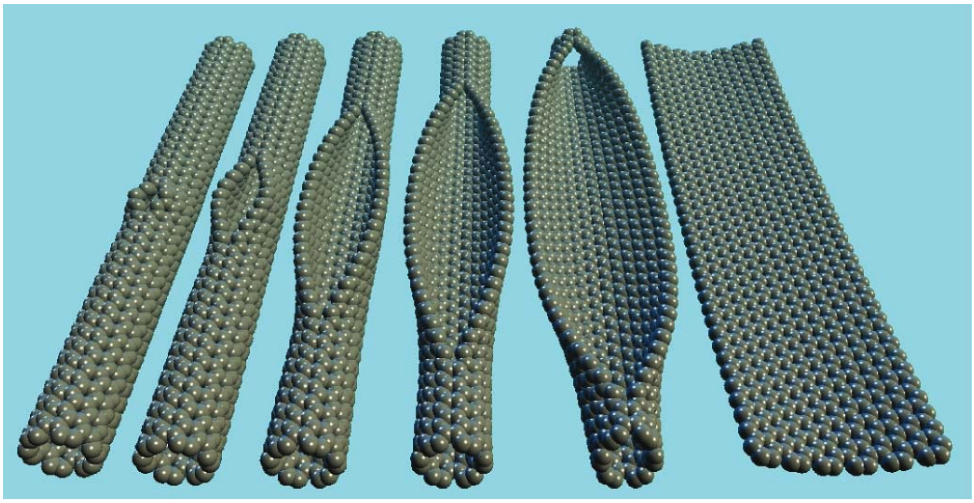

Figure 1.10: Schematic representation of unzipping nanotubes. (Adapted from [1]).

GNR structures: an armchair ribbon of width $N = 7$ (where N is the number of carbon atoms) obtained from $10,109 - dibromo - 9,99 - bianthryl$ precursor monomers and a "chevron" structure with a saw-tooth edge with alternating widths of $N = 6$ and $N = 7$ using $6,11 - dibromo - 1,2,3,4 - tetraphenyltriphenylene$ precursor monomers. The method that they used to obtain these ribbons consists of thermal sublimation of the monomers onto a metal surface of gold or silver. In this surface, the molecules easily lose their halogens and the surface is then heated in two steps. Firstly, at $200°C$, the dehalogenated blocks diffuse along the surface and the result is the formation of single covalent $C - C$ bonds between the monomers, creating polymer chains. In a second step, at $400°C$, the chain undergo cyclodehydrogenation and we observe the formation of an armchair edged ribbon. At the Fig. 1.11 we shown the scheme of this method to achievement of ribbons with armchair edges. In Fig. 1.12 we shown the comparison between experiment and theory, and we can see how this structures is obtained with a perfect atomic precision.

These experimental advantages in the study of nanostructures is very important, since the science is not made only of theories. Theory and experiments always go side-by-side. It is the experiment that validates a theory and theoretical explanations are an important tool in the study because they give many ideas for experiments about what paths to follow on the steps of the studies.

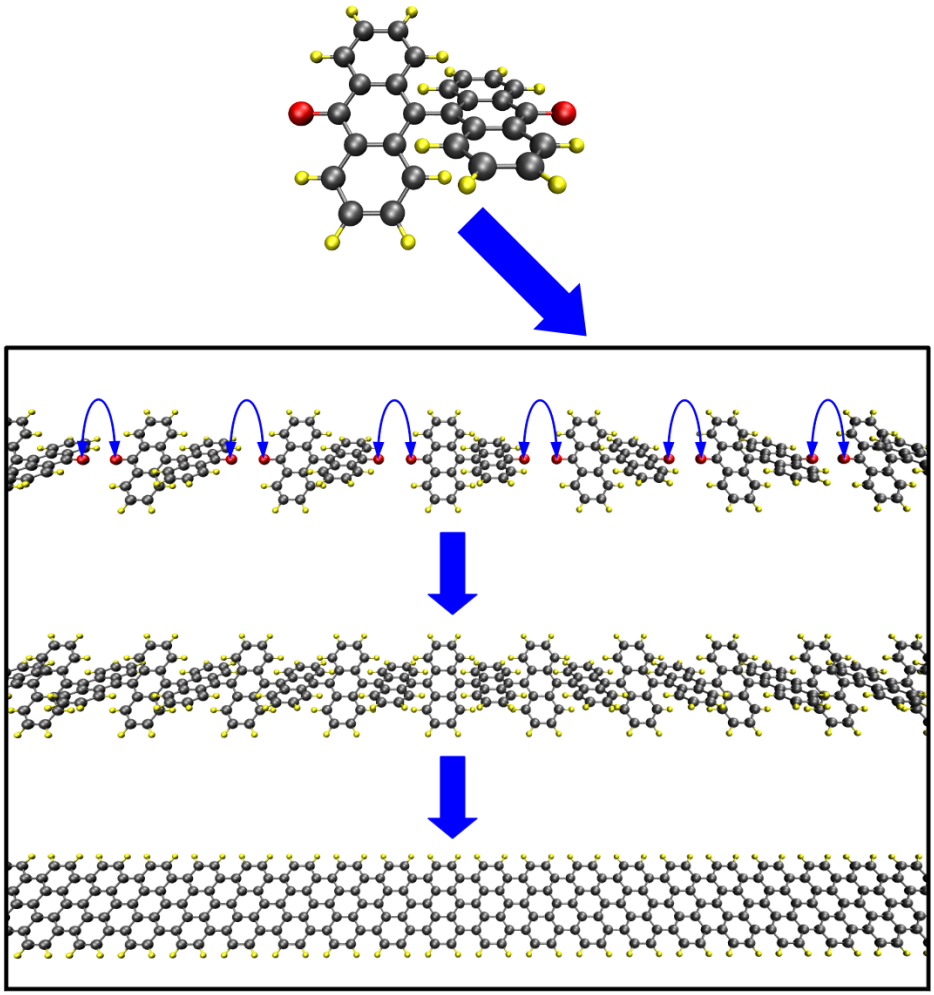

Figure 1.11: Schematic representation of bottom-up fabrication of atomically precise GNRs. (Adapted from [2]).

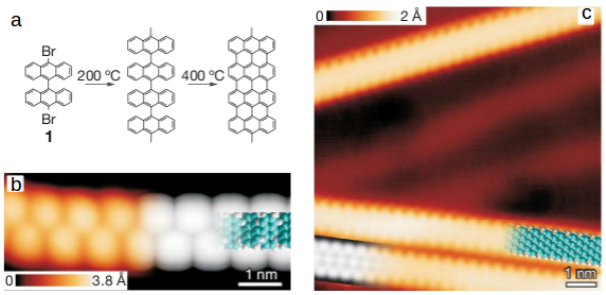

Figure 1.12: Reaction scheme to achievement straight $N = 7$ GNRs (a), STM image taken before the final cyclodehydrogenation step, and DFT-based simulation of the STM image (right) (b), high-resolution STM image with partly overlaid molecular model (blue) of the ribbon (c) (Adapted from [2]).

2 Methods

In this chapter we will talk about the methods used to calculate the electronic structure. First, we will present the Hamiltonian used to describe molecules and solids and introduce the approximate methods to solve them, given that it is impossible solve them analytically. In the following we will discuss the Bloch theorem and after talk about the tight-binding method that is employed for describing the Hamiltonian is our calculations. We will dedicate a section to talk about the Hubbard model that is used to solve problems involving the spin.

2.1 Hamiltonian

The physics properties of molecular systems are extracted solving the time dependent Schrödinger equation,

$$\hat{H}\psi = -i\hbar\frac{\partial}{\partial t}\psi. \tag{2.1}$$

The system Hamiltonian ($\hat{H}$), used for calculating the electronic structure of molecules and solids, is written as,

$$\begin{aligned}\hat{H} = \; & -\frac{\hbar^2}{2m}\sum_i \nabla_i^2 - \sum_I \frac{\hbar^2}{2M_I}\nabla_I^2 \\ & + \frac{1}{8\pi\epsilon_0}\sum_{i,j\ (i\neq j)}\frac{e^2}{|\mathbf{r}_i-\mathbf{r}_j|} + \frac{1}{8\pi\epsilon_0}\sum_{I,J\ (I\neq J)}\frac{Z_I Z_J e^2}{|\mathbf{r}_I-\mathbf{r}_J|} - \frac{1}{4\pi\epsilon_0}\sum_{i,I}\frac{Z_I e^2}{|\mathbf{r}_i-\mathbf{r}_I|},\end{aligned} \tag{2.2}$$

where i, j represent the electrons and I, J represent the atomic nuclei. The quantities $\mathbf{r}_i$ ($\mathbf{r}_I$), m_i (M_I) and Z_I represent respectively, the position of electrons (nucleus), the mass of electrons (nucleus) and the atomic number, while $\hbar$, ϵ_0 and e are the Plank's constant divided to 2π, permissibility of free space constant and the electron charge. The terms $-\frac{\hbar^2}{2m}\sum_i \nabla_i^2$ and $-\sum_I \frac{\hbar^2}{2M_I}\nabla_I^2$ represent the kinetic energy of electrons and nucleus, and finally, $\frac{1}{8\pi\epsilon_0}\sum_{i,j\ (i\neq j)}\frac{e^2}{|\mathbf{r}_i-\mathbf{r}_j|}$ ($\frac{1}{8\pi\epsilon_0}\sum_{I,J\ (I\neq J)}\frac{Z_I Z_J e^2}{|\mathbf{r}_I-\mathbf{r}_J|}$) and $-\frac{1}{4\pi\epsilon_0}\sum_{i,I}\frac{Z_I e^2}{|\mathbf{r}_i-\mathbf{r}_I|}$ represent the energy of interaction between electrons (nucleus) and and between electron-nuclei [21].

The inverse mass of the nuclei $\frac{1}{M_I}$ in the general Hamiltonian is small and so a perturbation series with general validity can be written in terms of this parameter. This way

the kinetic energy of nuclei is small compared to the other Hamiltonian contributions and can be ignored. This is the so called Born-Oppenheimer (BO) or adiabatic approximation, which is an excellent approximation for many purposes such as for the calculation of nuclear vibration modes in most solids [21]. Neglecting the nuclear kinetic energy, the fundamental Hamiltonian for the theory of electronic structure can be written as

$$\hat{H}\psi = \hat{T} + \hat{V_{ext}} + \hat{V_{int}} + E_{II}. \tag{2.3}$$

If we adopt the atomic units $\hbar = m_e = e = \frac{4\pi}{\epsilon_0} = 1$, the kinetic energy operator for the electrons $\hat{T}$ is

$$\hat{T} = \sum_i -\frac{1}{2}\nabla_i^2, \tag{2.4}$$

$\hat{V_{ext}}$ is the potential acting on the electrons due to the nuclei,

$$\hat{V_{ext}} = \sum_{i,I} V_I(|\mathbf{r}_i - \mathbf{R}_I|), \tag{2.5}$$

$\hat{V_{int}}$ is the electron-electron interaction,

$$\hat{V_{int}} = \frac{1}{2}\sum_{i\neq j} \frac{1}{|\mathbf{r}_i - \mathbf{r}_j|}, \tag{2.6}$$

and the final term E_{II} is the classical interaction nuclei-nuclei. Hence, this approximation allow us to decouple the nuclear and electronic problem.

2.2 Independent-electron approximation

Using BO approximation we simplify the original problem, but the problem remains complex and complicated to solve. So another approximation may be taken. The independent-electron approximation is widely used in theoretical calculations on the electronic structure of molecules and solids and allows us to write a Schrödinger-like equation for each electron separately. This approximation do not totally neglects the electron-electron interaction since the effects of others electrons can be described in the Schrödinger equation. There are different methods that use this approximation such as Hartree, Hartree-Fock, DFT (that is an exact method and not a approximation) and Tight-Binding. These methods differ each other by the form that the electron-electron interactions is inserted in the one-electron Schrödinger equation. Complementary methods are cited in Appendix A.

2.3 Bloch's theorem

In a perfect crystal, the ions are arranged in a regular periodic array. So, we can consider the problem of an electron in a potential $U(\mathbf{r})$ with the periodicity of the Bravais lattice,

$$U(\mathbf{r} - \mathbf{R}) = U(\mathbf{r}), \tag{2.7}$$

for all Bravais lattice vectors $\mathbf{R}$. If $\psi(\mathbf{r})$ and $\psi(\mathbf{r} + \mathbf{R})$ are the wavefunctions in $\mathbf{r}$ and $\mathbf{r} + \mathbf{R}$ respectively, we have,

$$|\psi_{n\mathbf{k}}(\mathbf{r} + \mathbf{R})|^2 = |\psi_{n\mathbf{k}}(\mathbf{r})|^2, \tag{2.8}$$

in other words, these functions differ from each other only for a global fase, $e^{i\mathbf{k}.\mathbf{R}}$,

$$\psi_{n\mathbf{k}}(\mathbf{r} + \mathbf{R}) = e^{i\mathbf{k}.\mathbf{R}}\psi_{n\mathbf{k}}(\mathbf{r}). \tag{2.9}$$

This is the Bloch Theorem [22]. The function $\psi_{n\mathbf{k}}(\mathbf{r})$ can be written as

$$\psi_{n\mathbf{k}}(\mathbf{r}) = e^{i\mathbf{k}.\mathbf{r}}u_{n\mathbf{k}}(\mathbf{r}), \tag{2.10}$$

where $u_{n\mathbf{k}}(\mathbf{r})$ is a function that has the lattice periodicity. In these equations, $\mathbf{k}$ is a vector of the reciprocal space and n enumerates different energy levels allowed for each $\mathbf{k}$. An important result is that two states corresponding to vectors $\mathbf{k}$ and $\mathbf{k}'$ that differ each other for a vector $\mathbf{K}$ of the reciprocal lattice are equivalent. As a consequence, we can map all possible states in a unitary cell of the reciprocal lattice (first Brillouin zone). In others words, the electronic structure of the material can be represented by plotting the eigenvalues of energy as a function of the vector $\mathbf{k}$ inside this zone. The Bloch theorem allow us to write the electronic problem of a periodic system in a convenient way to solve it, that is what we will do in the next section using Tight-Binding method.

2.4 Tight-Binding method

The tight-binding model (TB model) is an approach used for calculations of the electronic structures. This method uses an approximate set of wave functions based on superposition of wave functions for isolated atoms located at each atomic site. This method was developed by Bloch [23] in 1928. Tight-binding is applied to a wide variety of solids and gives good results.

In a crystalline solid, the translational symmetry along the directions of the lattice

vectors $\mathbf{a}_i$, makes that any wavefunction of the lattice satisfying the Bloch's theorem. In others words,

$$\hat{T}\Psi_k(\mathbf{r}) = e^{i\mathbf{k}.\mathbf{a}_i}\Psi_k(\mathbf{r}), \qquad (i = 1, \cdots, n) \tag{2.11}$$

where $\hat{T}$ is the translation operator along the lattice vector $\mathbf{a}_i$, and $\mathbf{k}$ is the Bloch wave vector [7]. The wave function can be defined in variety of models, but the most commonly used form is a linear combination of atomic orbitals. Thus the wave function $\Phi_j(\mathbf{k}, \mathbf{r})$ is defined as a summation on the atomic wavefunction $\varphi_j(\mathbf{r} - \mathbf{R})$,

$$\Phi_{j\mathbf{k}}(\mathbf{r}) = \frac{1}{\sqrt{N}} \sum_{\mathbf{R}}^{N} e^{i\mathbf{k}\cdot\mathbf{R}}\varphi_j(\mathbf{r} - \mathbf{R}), \qquad (j = 1, \cdots, n), \tag{2.12}$$

where $\mathbf{R}$ is the atom position and N is the number of atomic wavefunctions at the unit cell. We can verify, easily, that this function satisfies the Bloch condition

$$\begin{aligned} \Phi(\mathbf{k}, \mathbf{r} + \mathbf{a}) &= \frac{1}{\sqrt{N}} \sum_{\mathbf{R}}^{N} e^{i\mathbf{k},\mathbf{R}}\varphi_j(\mathbf{r} + \mathbf{a} - \mathbf{R}) \\ &= e^{i\mathbf{k}.\mathbf{a}} \frac{1}{\sqrt{N}} \sum_{\mathbf{R}-\mathbf{a}}^{N} e^{i\mathbf{k},(\mathbf{R}-\mathbf{a})}\varphi\Big[\mathbf{r} - (\mathbf{R} - \mathbf{a})\Big] \\ &= e^{i\mathbf{k}.\mathbf{a}}\Phi_j(\mathbf{k}, \mathbf{r}). \end{aligned} \tag{2.13}$$

The wavefunctions $\Psi_j(\mathbf{k}, \mathbf{r})$ in a solid, are expressed as a linear combination of the Bloch's functions,

$$\Psi_j(\mathbf{k}, \mathbf{r}) = \sum_{j'=1}^{n} C_{jj'}(\mathbf{k})\Phi'_j(\mathbf{k}, \mathbf{r}), \tag{2.14}$$

where $C_{jj'}$ are coefficients to be determined. The eigenvalues $E_j(\mathbf{k})$ is given by

$$E_j(\mathbf{k}) = \frac{\langle\Psi_j|H|\Psi_j\rangle}{\langle\Psi_j|\Psi_j\rangle} = \frac{\int \Psi_j^* \; H \; \Psi_j d\mathbf{r}}{\int \Psi_j^*\Psi_j d\mathbf{r}}. \tag{2.15}$$

Inserting Eq. (2.14) into Eq. (2.15), we obtain an expression for the energy

$$E_i(\mathbf{k}) = \frac{\sum_{j,j'=1}^{n} C_{ij}^* C_{ij'}\langle\Phi_j|H|\Phi_{j'}\rangle}{\sum_{j,j'=1}^{n} C_{ij}^* C_{ij'}\langle\Phi_j|\Phi_{j'}\rangle} = \frac{\sum_{j,j'=1}^{n} H_{jj'}(\mathbf{k})C_{ij}^* C_{ij'}}{\sum_{j,j'=1}^{n} S_{jj'}(\mathbf{k})C_{ij}^* C_{ij'}}, \tag{2.16}$$

where $H_{jj'}(\mathbf{k})$ and $S_{jj'}(\mathbf{k})$ are the transfer and overlap matrices, respectively. We can write these Hamiltonian elements in Bloch's functions basis. The advantage of using this basis is that we redirect our attention from a set of infinite vectors R in real space to a set of finite vectors k of the reciprocal space (determined by the Brillouin zone), moreover, the

Hamiltonian is block diagonal and the diagonalization can be broken in small matrices. We will write the Hamiltonian elements of the Bloch's functions in terms of the "old" basis (atomic orbitals basis), because we know to operate in this basis. The elements of the Hamiltonian in terms of this basis can be written as

$$\begin{aligned}
\langle\Phi_j|\hat{H}|\Phi_{j'}\rangle &= \frac{1}{N}\int d^3\mathbf{r}\Phi^*_{j\mathbf{K}'}(\mathbf{r})\hat{H}\Phi_{l\mathbf{K}''}(\mathbf{r}) \\
&= \frac{1}{N}\int d^3\mathbf{r}\left(\sum_{\mathbf{R}'} e^{-i\mathbf{k}'.\mathbf{R}'}\varphi^*_j(\mathbf{r}-\mathbf{R}')\right)\hat{H}\left(\sum_{\mathbf{R}''} e^{i\mathbf{k}''.\mathbf{R}''}\varphi_l(\mathbf{r}-\mathbf{R}'')\right) \\
&= \frac{1}{N}\sum_{\mathbf{R}'} e^{-i\mathbf{k}'.\mathbf{R}'}\sum_{\mathbf{R}''} e^{i\mathbf{k}''.\mathbf{R}''}\int d^3\mathbf{r}\varphi^*_j(\mathbf{r}-\mathbf{R}')\hat{H}\varphi_l(\mathbf{r}-\mathbf{R}'') \\
&= \frac{1}{N}\sum_{\mathbf{R}'} e^{-i\mathbf{k}'.\mathbf{R}'}\sum_{\mathbf{R}''} H_{j,l}(\mathbf{R}''-\mathbf{R}') \\
&= \frac{1}{N}\sum_{\mathbf{R}'} e^{-i\mathbf{k}'.\mathbf{R}'}e^{i\mathbf{k}'.\mathbf{R}'}\left(\sum_{\mathbf{R}''} e^{i\mathbf{k}'.(\mathbf{R}''-\mathbf{R}')}H_{j,l}(\mathbf{R}''-\mathbf{R}')\right) \\
&= \frac{1}{N}\sum_{\mathbf{R}'} e^{-i\mathbf{k}'.\mathbf{R}'}e^{i\mathbf{k}'.\mathbf{R}'}H_{j,l}(\mathbf{k}') \\
&= H_{j,l}(\mathbf{k}')\frac{1}{N}\sum_{\mathbf{R}'} e^{-i\mathbf{k}'.\mathbf{R}'}e^{i\mathbf{k}'.\mathbf{R}'} \\
&= H_{j,l}(\mathbf{k}')\delta_{\mathbf{k}\mathbf{k}'}, \qquad (2.17)
\end{aligned}$$

and finally, the Hamiltonian elements and the overlap matrix elements are, respectively

$$H_{j,l}(\mathbf{k},\mathbf{k}) = H_{j,l}(\mathbf{k}) = \sum_{\mathbf{R}} e^{i\mathbf{k}.\mathbf{R}}H_{j,l}(\mathbf{R}), \qquad (2.18)$$

$$S_{j,l}(\mathbf{k},\mathbf{k}) = S_{j,l}(\mathbf{k}) = \sum_{\mathbf{R}} e^{i\mathbf{k}.\mathbf{R}}S_{j,l}(\mathbf{R}). \qquad (2.19)$$

The eigenfunctions can be expanded as a linear combination of Bloch's function

$$\Psi_\alpha(\mathbf{r}) = \sum_j c_{j\alpha}\Phi_{j\mathbf{k}}(\mathbf{r}), \qquad (2.20)$$

and the Schrödinger equation in the LCAO basis reads

$$\sum_j = c_{j\alpha}\hat{H}\Phi_{j\mathbf{k}}(\mathbf{r}) = E_\alpha\sum_j c_{j\alpha}\Phi_{j\mathbf{k}}(\mathbf{r}), \qquad (2.21)$$

multiplying on the left by $\Phi^*_{j\mathbf{k}}(\mathbf{r})$ and integrating we have the secular equation

$$\begin{aligned}\sum_j = c_{j\alpha}\int d^3\mathbf{r}\Phi^*_{j\mathbf{k}}(\mathbf{r})\hat{H}\Phi_{j\mathbf{k}}(\mathbf{r}) &= E_\alpha \sum_{jc_{j\alpha}}\int d^3\mathbf{r}\Phi^*_{j\mathbf{k}}(\mathbf{r})\Phi_{j\mathbf{k}}(\mathbf{r}),\\ \sum_j c_{j\alpha}H_{l,j}(\mathbf{k}) &= \sum_j c_{j\alpha}E_\alpha S_{l,j}(\mathbf{k}),\\ (\mathbf{H} &- E_\alpha\mathbf{S})c_\alpha = 0. \end{aligned} \tag{2.22}$$

Where $\mathbf{H}$ and $\mathbf{S}$ are square matrices with elements $H_{l,j}(\mathbf{k})$ and $S_{l,j}(\mathbf{k})$ and c_α is a column vector. In order to have non-trivial solutions, the determinant has to be zero

$$|\mathbf{H} - E_\alpha\mathbf{S}| = 0. \tag{2.23}$$

This is the secular equation, the eigenvalues E_α give the energy of electronic bands. Writing the secular equation in matrix form

$$\begin{vmatrix} \mathbf{H}(\mathbf{k}_1) - E_\alpha\mathbf{S}(\mathbf{k}_1) & 0 & 0 & ... & 0 \\ 0 & \mathbf{H}(\mathbf{k}_2) - E_\alpha\mathbf{S}(\mathbf{k}_2) & 0 & ... & 0 \\ 0 & 0 & \mathbf{H}(\mathbf{k}_3) - E_\alpha\mathbf{S}(\mathbf{k}_3) & ... & 0 \\ . & . & . & . & . \\ . & . & . & . & . \\ . & . & . & . & . \\ 0 & 0 & 0 & ... & \mathbf{H}(\mathbf{k}_N) - E_\alpha\mathbf{S}(\mathbf{k}_N) \end{vmatrix} = 0, \tag{2.24}$$

we see easily that the problem can be solved diagonalizing each block separately.

In our calculations, we use the parametrization proposed by Gunlicke [17], where $\gamma_1 = -3,2\ eV$, $\gamma_2 = 0\ eV$ e $\gamma_3 = -0,3\ eV$ for the hopping integers between first, second and thirds neighbors, respectively as illustrated in Fig 2.1. The atomic configuration for the edges atoms is different in comparison with the atoms within the system and we insert a correction $\triangle\gamma_1 = -0,2\ eV$ at the γ_1 parameter for these atoms [17].

2.5 Graphene

The graphene's unit cell is composed by two atoms we will call A and B. For this section we consider only interactions between first neighbors atoms, so we have a 2x2 Hamiltonian,

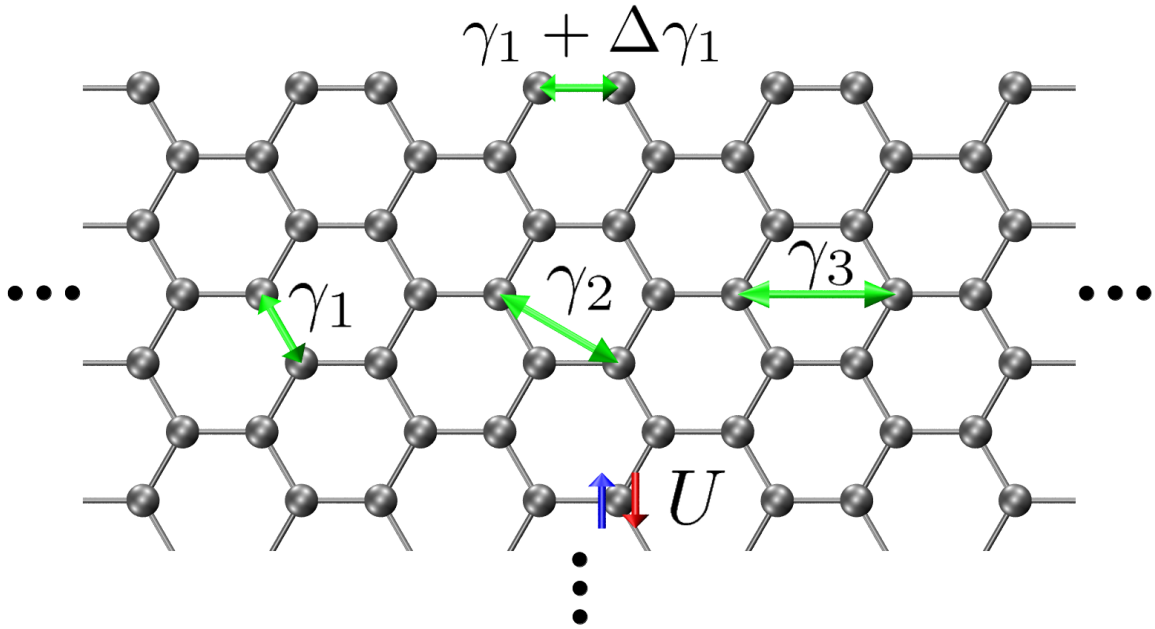

Figure 2.1: Schematic representation of first, second and thirds neighbors in an armchair graphitic structure.

$$\mathbf{H} = \begin{bmatrix} H_{AA} & H_{AB} \\ H_{BA} & H_{BB} \end{bmatrix}. \tag{2.25}$$

In this calculation what matters is the relative position $\mathbf{R}$ between the cells of each atom, so we consider that the first atom is localized at the $\mathbf{R} = 0$. Using the Eq.(2.4) we can calculate this Hamiltonian's elements,

$$\langle \Phi_A | \hat{H} | \Phi_A \rangle = \sum_R e^{i\mathbf{k}\cdot\mathbf{R}} H_{AA}(\mathbf{R}), \tag{2.26}$$

since A has not B as first neighbor, in this somatory the only term that survive is the element A with himself, that is the site energy, the same occurs for the element B, so we have that

$$\langle \Phi_A | \hat{H} | \Phi_A \rangle = \epsilon_{2p}, \tag{2.27}$$

$$\langle \Phi_B | \hat{H} | \Phi_B \rangle = \epsilon_{2p}. \tag{2.28}$$

The Hamiltonians elements H_{AB} and H_{BA} are

$$\begin{aligned}\langle\Phi_A|\hat{H}|\Phi_B\rangle &= \sum_R e^{i\mathbf{k}\cdot\mathbf{R}} H_{AB}(\mathbf{R}) \\ &= \gamma + e^{-i\mathbf{k}\cdot\mathbf{a}_1}\gamma + e^{-i\mathbf{k}\cdot\mathbf{a}_2}\gamma \\ &= \gamma(1 + e^{-i\mathbf{k}\cdot\mathbf{a}_1} + e^{-i\mathbf{k}\cdot\mathbf{a}_2}) \\ &= \gamma f(\mathbf{k}). \end{aligned} \tag{2.29}$$

$$\begin{aligned}\langle\Phi_B|\hat{H}|\Phi_A\rangle &= \sum_R e^{i\mathbf{k}\cdot\mathbf{R}} H_{BA}(\mathbf{R}) \\ &= \gamma + e^{i\mathbf{k}\cdot\mathbf{a}_1}\gamma + e^{i\mathbf{k}\cdot\mathbf{a}_2}\gamma \\ &= \gamma(1 + e^{i\mathbf{k}\cdot\mathbf{a}_1} + e^{i\mathbf{k}\cdot\mathbf{a}_2}) \\ &= \gamma f(\mathbf{k})^*. \end{aligned} \tag{2.30}$$

Where $\mathbf{a}_1$ and $\mathbf{a}_2$ are the graphene's lattice vector (see equation 1.6). This way, we have

$$\mathbf{H} = \begin{bmatrix} \epsilon_{2p} & \gamma f(\mathbf{k}) \\ \gamma f(\mathbf{k})^* & \epsilon_{2p} \end{bmatrix}. \tag{2.31}$$

The overlap matrix S_{ij} can be calculated by a similar method as used for H_{ij}, except that the intra-atomic integral yields the unity for the case of normalized basis functions, so that $S_{AA} = S_{BB} = 1$, $S_{AB} = sf(\mathbf{k})$ and $S_{BA} = sf(\mathbf{k})^*$, where s is the overlap integral between the nearest A and B atoms,

$$s = \langle\varphi_A(\mathbf{R})|\varphi_B(\mathbf{R})\rangle, \tag{2.32}$$

so, $\mathbf{S}$ can be written as

$$\mathbf{S} = \begin{bmatrix} 1 & \gamma s(\mathbf{k}) \\ \gamma s(\mathbf{k})^* & 1 \end{bmatrix}. \tag{2.33}$$

Solving the secular equation $|\mathbf{H} - E\mathbf{S}| = 0$, the eigenvalues $E(\mathbf{k})$ are obtained as a function $\omega(\mathbf{k})$, k_x and k_y

$$\begin{aligned}\mathbf{k}\cdot\mathbf{a}_1 &= k_x\frac{a\sqrt{3}}{2} + k_y\frac{a}{2}, \\ \mathbf{k}\cdot\mathbf{a}_2 &= k_x\frac{a\sqrt{3}}{2} - k_y\frac{a}{2}, \end{aligned} \tag{2.34}$$

this way $f(\mathbf{k})$ can be written as

$$f(\mathbf{k}) = 1 + e^{-ik_x \frac{a\sqrt{3}}{2}} e^{-ik_y \frac{a}{2}} + e^{-ik_x \frac{a\sqrt{3}}{2}} e^{ik_y \frac{a}{2}}, \tag{2.35}$$

and finally

$$E_{g2D}(\mathbf{k}) = \frac{\epsilon_{2p} \pm \gamma\omega(\mathbf{k})}{1 \pm s\omega(\mathbf{k})}, \tag{2.36}$$

where the + signs in the numerator and denominator go together giving the bonding π energy band, and likewise for the − signs, which give the anti-bonding π^* band, while the function $f(\mathbf{k})$ is given by

$$f(\mathbf{k}) = \sqrt{1 + 4\cos\left(\frac{\sqrt{3}k_x a}{2}\right)\cos\left(\frac{k_y a}{2}\right) + 4\cos^2\left(\frac{k_y a}{2}\right)}. \tag{2.37}$$

When the overlap integral s becomes zero, the π and π^* bands become symmetrical around $E = \epsilon_{2p}$. The energy dispersion relations in the case of $s = 0$ are commonly used as a simple approximation for the electronic structure of a graphene layer

$$E_{g2D}(k_x, k_y) = \pm\gamma\left[1 + 4\cos\left(\frac{\sqrt{3}k_x a}{2}\right)\cos\left(\frac{k_y a}{2}\right) + 4\cos^2\left(\frac{k_y a}{2}\right)\right]^{\frac{1}{2}}. \tag{2.38}$$

2.6 Hubbard model

Graphitic materials with zigzag edges have a electronic spin polarization, so we have to consider the interaction between spins. A simple model which is widely used for studying the magnetic effects considering the spin-spin interactions is the Hubbard model [24]. In this model, the Hamiltonian is written as a sum of two parts

$$\hat{H} = \hat{H}_0 + \hat{H}', \tag{2.39}$$

where, the first Hamiltonian $\hat{H}_0$ is the usual tight-binding Hamiltonian and $\hat{H}'$ is the Hubbard Hamiltonian given by

$$\hat{H}_U = U \sum_i \hat{n}_i^{\uparrow} \hat{n}_i^{\downarrow}, \tag{2.40}$$

where $\hat{n}_{i\sigma} = c_{i\sigma}^{\dagger} c_{i\sigma}$ and $c_{i\sigma}^{\dagger}$ and $c_{i\sigma}$ are the creation and annihilation operators, respectively, at site i. The parameter $U > 0$ defines the magnitude of the on-site Coulomb repulsion and it is obtained from first principles calculations. We used $U = 0,92\gamma_1$ in our

calculations [25]. Using a mean-field approximation, we can write $\hat{H}'$ as

$$\hat{H}_U = U \sum_i (\langle \hat{n}_i^{\uparrow} \rangle \hat{n}_i^{\downarrow} + \hat{n}_i^{\downarrow} \langle \hat{n}_i^{\uparrow} \rangle), \tag{2.41}$$

where the densities $\langle \hat{n}_i^{\uparrow} \rangle$ and $\langle \hat{n}_i^{\downarrow} \rangle$ are determined self-consistently [24, 26].

3 Electronic transport

Our purpose in this chapter is to describe the electronic transport at the nanoscale. We start talking about the Landauer formalism and then we will describe the general system used to study the electronic transport.

3.1 Quantum currents

The probability current $J(x,t)$ in 1D is defined as

$$J(x,t) = \frac{i\hbar}{2m}\left(\Psi\frac{\partial\Psi^*}{\partial x} - \Psi^*\frac{\partial\Psi}{\partial x}\right). \tag{3.1}$$

This definition is such that

$$\frac{dP_{ab}(t)}{dt} = J(a,t) - J(b,t) \tag{3.2}$$

describes the change in the probability $P_{ab}(t)$ of finding a particle in a region $a < x < b$ at time t, where

$$P_{ab}(t) = \int_a^b |\Psi(x,t)|^2 dx. \tag{3.3}$$

Setting $b = a + dx$, allows one to write Eq. 3.1 as

$$\frac{\partial\rho(x,t)}{\partial t} = -\frac{\partial J(x,t)}{\partial x}, \tag{3.4}$$

with $\rho(x,t) = |\Psi(x,t)|^2$ the probability density. This equation can be recognized as a continuity equation, which describes the relation between a density and a current.

Suppose the particle has a charge q. Then the expected charge found in the region $a < x < b$ at time t is $Q_{ab}(t) = qP_{ab}(t)$. Defining the electrical current as $I(x,t) = qJ(x,t)$, Eq. 3.1 can be rewritten as

$$\frac{aQ_{ab}(t)}{dt} = I(a,t) - I(b,t). \tag{3.5}$$

This makes sense, the rate of charge is given by the difference between the current flowing in from one side minus the current flowing out from the other side.

Suppose now that $\Psi(x,t)$ describes a stationary state,

$$\Psi(x,t) = \psi(x)e^{-\frac{i}{\hbar}Et}, \tag{3.6}$$

we find from Eq. 3.1

$$\frac{dP_{ab}(t)}{dt} = 0 \tag{3.7}$$

and consequently from Eqs. 3.1 and 3.1

$$J(x,t) = J = constant. \tag{3.8}$$

The probability current is constant, independent of position and time.

Consider the scattering problem shown in Fig. 3.1. In the left and in the right regions,

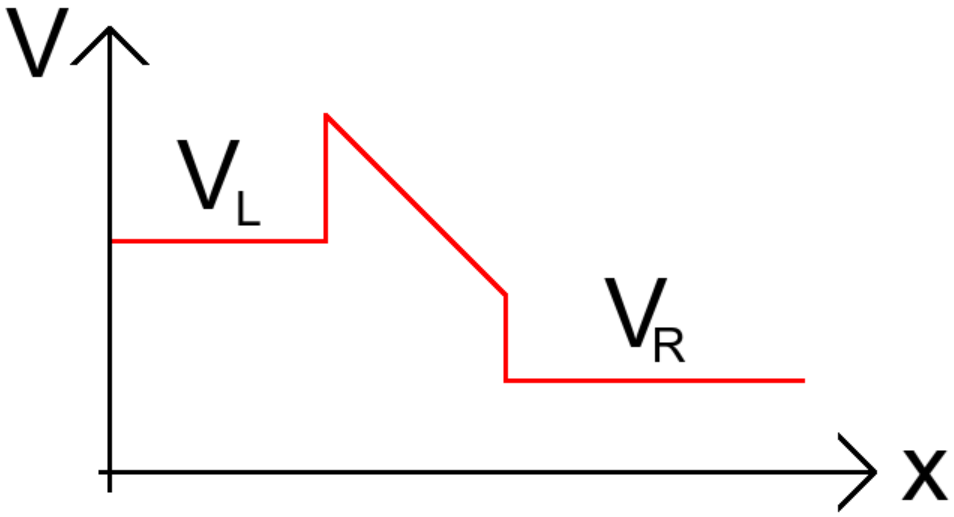

Figure 3.1: Illustrative example for a scaterring problem.

the potential $V(x)$ is constant and equal to V_L and V_R, respectively. In the middle region the potential can be any shape. The solution in the left region is

$$\psi(x) = Ae^{ik_L x} + Be^{-ik_L x}, \tag{3.9}$$

with

$$K_L = \frac{\sqrt{2m(E-V_L)}}{\hbar}. \tag{3.10}$$

The solution in the right region is given by the transmitted wave

$$\psi(x) = Fe^{iK_R x}, \tag{3.11}$$

with

$$K_R = \frac{\sqrt{2m(E-V_R)}}{\hbar}. \tag{3.12}$$

The transmission coefficient T is defined as the ratio between transmitted and incident currents

$$T = \frac{J_T}{J_{in}} = \frac{v_R}{v_L}\frac{|F|^2}{|A|^2}. \tag{3.13}$$

From the fact that the current has to be independent of position, we have

$$\begin{aligned} J_T &= J_{in} - J_R \\ J_{in} &= J_R + J_T, \end{aligned} \tag{3.14}$$

this relation expresses the conservation of current.

3.2 System description

The system used to study the electronic transport in nanoscale is composed by a central scattering region (CSR) connected with a number N of semi-infinite terminals as shown in Fig. 3.2. Each terminal is composed by the repetition of unit cell in a periodic direction.

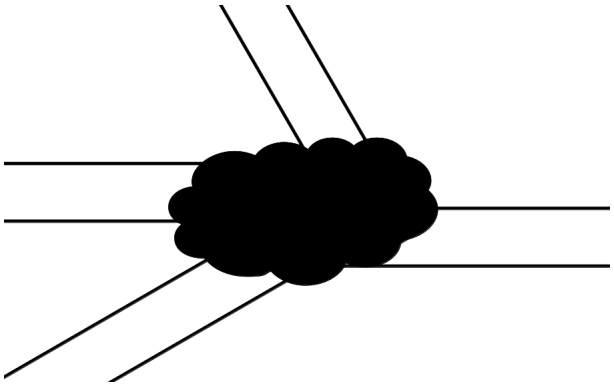

Figure 3.2: Setup for the basic system investigated in electronic transport calculations.

We apply the concept of principal layer (PL) to the electrodes. In other words, the terminal's unit cell interacts only with the first-neighbor cells, that allow us to write the problem in a numerical solvable way. So we can describe the terminals using semi-infinite matrices Hamiltonians. We label the unit cells within each terminal by the integer i where for the cell closest to the CSR $i = 0$ as shown in Fig. 3.3.

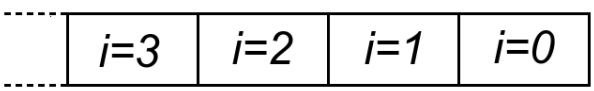

Figure 3.3: Labeling of the unit cells from a semi-infinite terminal.

The matrix H_i^n describes the unit cell for the i-th terminal and $H_{i,j}^n$ describe the interaction between the terminal cells i and j. According to the PL condition $H_{i,j}^n$ only

will be nonzero if i and j are first-neighbors. Under these conditions we can write the Hamiltonian H_n corresponding to the n-th terminal as

$$H_n = \begin{bmatrix} H_0^n & H_{01}^n & 0 & 0 & ... \\ H_{10}^n & H_1^n & H_{12}^n & 0 & ... \\ 0 & H_{21}^n & H_2^n & H_{23}^n & ... \\ \vdots & \vdots & \vdots & \vdots & \ddots \end{bmatrix}. \tag{3.15}$$

3.3 Quantum conductance

The quantum description of transport properties in nanoscale is given by the Landauer formalism [27, 28], which associates the quantum conductance $\mathcal{G}$ with the transmission probability $\mathcal{T}_{nm}$ of an electron to tunnel from a given terminal n to another terminal m by:

$$\mathcal{G} = \frac{e^2}{\hbar}\mathcal{T}_{nm} \tag{3.16}$$

where $\frac{e^2}{\hbar}$ is called the quantum of conductance. In order to calculate the quantum conductance we use the Green's function formalism [29], where the main quantity is the conductor Green's function G_C to be defined properly in the next section. According to this formalism, we can write the transmission function as:

$$\mathcal{T}_{nm} = Tr(\Gamma_n G_C^r \Gamma_m G_C^a) \tag{3.17}$$

where G_C^r and G_C^a are the retarded and advanced Green's functions for the conductor and Γ_p $(p = n, m)$ represent the coupling between the CSR and the terminal p. Such couplings are defined in terms of the terminal self-energy Σ_p (to be define in the next section) as

$$\Gamma_p = i(\Sigma_p - \Sigma_p^\dagger). \tag{3.18}$$

3.4 Green's function

Let us consider the single-particle Hamiltonian

$$H_S = -\frac{\hbar^2}{2m}\nabla^2 + V(\mathbf{r}) \tag{3.19}$$

consisting of the kinetic part, which we call $\hat{H}_0$, and the potential $\hat{V}$ describing the scattering due to the nanoscale junction. We can then solve the time-dependent Shrödinger equation

$$i\hbar\frac{d|\Psi(t)\rangle}{dt} = \hat{H}_S|\Psi(t)\rangle = (\hat{H}_0 + \hat{V}|\Psi(t)\rangle). \tag{3.20}$$

The above equation has the general form

$$\hat{L}\psi(t) = f(t) \tag{3.21}$$

with

$$\hat{L} = i\hbar\frac{d}{dt} - \hat{H}. \tag{3.22}$$

From the general theory of differential equations we then know that there exists a quantity, called *Green's function* or *propagator*, $\hat{G}(t)$, satisfying the equation of motion

$$\hat{L}\hat{G}(t) = \hat{1}\delta(t). \tag{3.23}$$

We can write the Schrödinger equation in terms of two types of Green's functions

$$\left(i\hbar\frac{\partial}{\partial t} - \hat{H}_S\right)\hat{G}^{\pm}(t) = \hat{1}\delta(t) \tag{3.24}$$

the Green's functions $\hat{G}^+$ and $\hat{G}^-$ have the following boundary conditions

$$\begin{aligned} \hat{G}^+(t) &= 0 \qquad t < 0 \qquad \text{retarded} \\ \hat{G}^-(t) &= 0 \qquad t > 0 \qquad \text{advanced.} \end{aligned} \tag{3.25}$$

These solutions can be written as

$$\hat{G}^+ = -\frac{i}{\hbar}e^{-i\hat{H}_S t/\hbar} \qquad t > 0 \tag{3.26}$$

$$\hat{G}^- = \frac{i}{\hbar}e^{-i\hat{H}_S t/\hbar} \qquad t < 0. \tag{3.27}$$

We note that $\hat{G}^+(t)$ is proportional to the time evolution operator $U(t, t_0)$ if the Hamiltonian does not depend on time, so that we can write

$$|\Psi(t)\rangle = i\hbar\hat{G}^+(t)|\Psi(0)\rangle \tag{3.28}$$

Analogously for the $\hat{G}^-(t)$, we can write

$$|\Psi(t)\rangle = -i\hbar\hat{G}^-(t)|\Psi(0)\rangle, \tag{3.29}$$

in other words, $\hat{G}^+$ propagates the wave function from a past time $t_0 = 0$ to a future time $t > 0$ (retarded), while $\hat{G}^-$ propagates $|\Psi\rangle$ backwards from a time $t_0 = 0$ to a past time $t < 0$ (advanced).

Once we have derived the time-dependent version to the GF, the corresponding time-independent can be easily obtained by Fourier transform

$$\begin{aligned}\hat{G}^{+}(E) &= \int dt e^{iEt/\hbar}\hat{G}^{+}(t) \\ &= \frac{i}{\hbar}\int dt e^{i(E-\hat{H})t/\hbar} \\ &= -\frac{1}{E-\hat{H}}e^{i(E-\hat{H})t/\hbar}\Big|_{0}^{\infty}\end{aligned} \tag{3.30}$$

We will insert a $i\eta$ ($\eta \to 0^{+}$) in order to avoid poles on the real axis for the energy, so we have [30]

$$\hat{G}^{+}(E) = \frac{1}{E+i\eta-\hat{H}}. \tag{3.31}$$

and similarly for the advanced function

$$\hat{G}^{-}(E) = \frac{1}{E-i\eta-\hat{H}}. \tag{3.32}$$

In order to make a connection with the Landauer formalism, we are going to consider the simplest problem that consist of a CSR with only one terminal, as shown in Fig. 3.4.

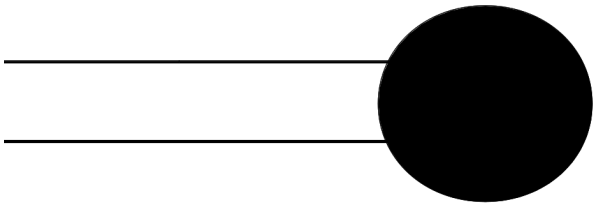

Figure 3.4: One terminal-system.

We can write the Hamiltonian as

$$H = \begin{bmatrix} H_C & H_{CT} \\ H_T & H_T \end{bmatrix}, \tag{3.33}$$

where H_C is the Hamiltonian of the CSR, $H_{CT} = H_{TC}^{\dagger}$ is the Hamiltonian that describes the interaction between the central region and the terminal and H_T is the Hamiltonian for terminal. We can re-write the Eq. 3.31 (or Eq. 3.32) in matrix form as

$$(\varepsilon\hat{1} - H) = \hat{1} \tag{3.34}$$

where $\varepsilon = E + i\eta(E - i\eta)$ for the retarded (advanced) GF. It follows

$$\begin{bmatrix} \varepsilon I_C - H_C & -H_{CT} \\ -H_{TC} & \varepsilon I_T - H_T \end{bmatrix} \cdot \begin{bmatrix} G_C & G_{CT} \\ G_{TC} & G_T \end{bmatrix} = \begin{bmatrix} I_C & 0 \\ 0 & I_T \end{bmatrix} \tag{3.35}$$

and making the product, we have

$$(\varepsilon I_C - H_C)G_C - H_{CT}G_{TC} = I_C \tag{3.36}$$

$$-H_{TC}G_C + (\varepsilon I_T - H_T)G_{TC} = 0. \tag{3.37}$$

Isolating G_{TC} in Eq. 3.37 we obtain

$$G_{TC} = (\varepsilon I_T - H_T)^{-1} H_{TC} G_C = g_T H_{TC} G_C, \tag{3.38}$$

where g_T is the GF for the isolated terminal. Replacing G_{TC} in Eq. 3.36 we have

$$(\varepsilon I_C - H_C - H_{CT} g_T H_{TC}) G_C = I_C. \tag{3.39}$$

Using $\Sigma_T = H_{CT} g_T H_{TC}$

$$G_C = (\varepsilon I_C - H_C - \Sigma_T)^{-1}. \tag{3.40}$$

The matrix Σ_T represents the self-energy of terminals, that can be viewed as a effective potential which describes the effects of the semi-infinite terminal on the finite CSR. This way we create a modified Hamiltonian that reduces the infinite system to a finite system, satisfying the same boundary conditions of the CSR attached to semi-infinite electrode.

Now, we can generalize this problem for a system that consisting of CSR attached to a number N of semi-infinite electrodes (Fig 3.2). Using Eq. 3.34 we have

$$\begin{bmatrix} \varepsilon I_C - H_C & -H_{C1} & -H_{C2} & \cdots & -H_{CN} \\ -H_{1C} & \varepsilon I_1 - H_1 & 0 & \cdots & 0 \\ -H_{2C} & 0 & \varepsilon I_2 - H_2 & \cdots & 0 \\ \vdots & \vdots & \vdots & \cdots & \vdots \\ -H_{NC} & 0 & 0 & \cdots & \varepsilon I_N - H_N \end{bmatrix} \cdot \begin{bmatrix} G_C & G_{C1} & G_{C2} & \cdots & G_{CN} \\ G_{1C} & G_{11} & G_{12} & \cdots & G_{1N} \\ G_{2C} & G_{21} & G_{22} & \cdots & G_{2N} \\ \vdots & \vdots & \vdots & \cdots & \vdots \\ G_{NC} & G_{N1} & G_{N2} & \cdots & G_{NN} \end{bmatrix} = \hat{1}. \tag{3.41}$$

Performing the product we have

$$(\varepsilon I_C - H_C)G_C - \sum_{i=1}^{N} H_{Ci} G_{iC} = I_C \tag{3.42}$$

$$G_{iC} = (\varepsilon I_i - H_i)^{-1} H_{iC} G_C. \tag{3.43}$$

Making $g_i = (\varepsilon I_i - H_i)^{-1}$

$$G_{iC} = g_i H_{iC} G_C \tag{3.44}$$

then, substituting Eq. 3.43 into Eq. 3.42 we have

$$(\varepsilon I_C - H_C - \sum_i H_{Ci} g_i H_{iC}) G_C = I_C. \tag{3.45}$$

Using a simplified notation for the terms in the sum ($\Sigma_i = H_{Ci} g_i H_{iC}$) we have

$$G_C = (\varepsilon I_C - H_C - \sum_i \Sigma_i)^{-1} \tag{3.46}$$

and finally

$$G_C = (\varepsilon I_C - H_C - \Sigma_1 - \Sigma_2 - \cdots - \Sigma_N)^{-1}. \tag{3.47}$$

In order to perform such calculations, we used a computational package used in previous studies [15]. The system Hamiltonian is written in terms of the tight-binding approach by using another package used previously [25].

4 Three-Terminals Graphitic Junctions

In this chapter we study the electronic transport properties of a series of three-terminal junctions composed of armchair edged GNRs (AGNRs). The junction geometry is based on a triangular shape obtained by the assembling of three finite pieces of AGNRs into an equilateral triangle. We investigate how details of this triangular arrangement influence the transport, as well as the mechanisms which arise from specific geometric connections of this central structure with the semi-infinite terminals [31].

4.1 Systems

The carbon structures considered here consist of three finite AGNR sections joined together into an equilateral triangle, as depicted in Fig. 4.1a. We will refer to these structures as triangular graphene nanoribbons (TGNRs). In the example shown in Fig. 4.1a, an AGNR with $N_{CC} = 11$ $C-C$ dimer lines along the ribbon's width (11-AGNR) is used to construct the TGNR arms. As two adjacent AGNR blocks make a 60° angle, such construction can be made free of pentagonal and heptagonal rings at the triangle apices. The size of the core structure is denoted by an integer N for the distance $\overline{12}$ (see Fig. 4.1a) in units of the a_{CC} bond distance in graphene. For the transport calculations we seamlessly attached three semi-infinite AGNR terminals to the corners of the TGNR in two distinct configurations: symmetric (Fig 4.1b) and non-symmetric (Fig 4.1c). In both cases, the connections to the terminals are made in such a way that the junctions remain benzoidal. This construction results in systems suitable to be supported over planar substrates due to the lack of curvature originating from, e.g., non-hexagonal carbon rings. We stress that the presence of curvature does not preclude the deposition of a material over a planar surface. In fact, curvature can play an important role in the growing of graphitic nanostructures by bottom-up synthesis approaches based on the assembling of molecules over plane substrates [2, 32, 33, 34, 35, 36], since (non) planar molecular building blocks present higher (lower) diffusion barriers, resulting in the growth of nanostructures with reduced (extended) sizes. Furthermore, once a given nanostructure is grown, absence of curvature

can enhance sample-substrate interactions, easing their deposition on surfaces and their assembly into complex extended circuits. Even though TGNRs have not been synthesized yet, current advances in the development of bottom-up preprogrammed routes for the construction of specific graphitic structures [36, 37, 38, 36], including multi-terminal junctions [2], lend support to the future feasibility of assembling carbon nanostructures with increasing complexity, including those presented here.

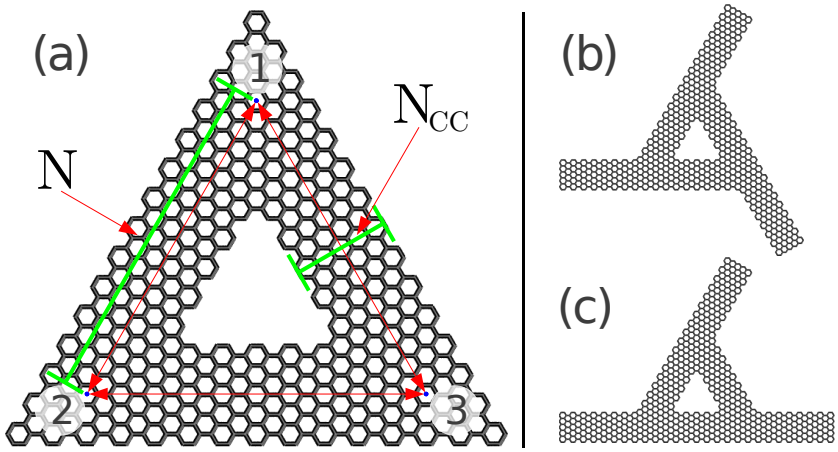

Figure 4.1: (a) Equilateral AGNR triangle (TGNR) composing the central scattering region for the studied systems. The systems size is denoted by the distance $\overline{12}$ in units of the carbon-carbon distance a_{CC} in graphene ($N = 30$ in this example) and we denoted how wide is the ribbon by the number of N_{CC} lines along its width. Symmetric and non-symmetric junction geometries, obtained by the fusion of GNR-made terminals with armchair edges, are illustrated in (b) and (c), respectively.

4.2 Numerical Results

First, we investigate the electronic structure of the TGNR with 11 $C-C$ lines corresponding to $N = 30$. In Fig. 4.2a we plot the density of states (DOS) along with partial charge density plots for the occupied states close to the Fermi energy. We label the four peaks in the energy interval $[-0.8\ eV, 0]$ from 1 to 4, starting with the one closest to $E_f = 0$. Peaks 2 and 3 have amplitudes half that of peaks 1 and 4 since the latter ones correspond to doubly degenerated electronic levels (not accounting for spin degeneracy) as confirmed by the independent tight-binding calculation performed for the isolated triangle. The twofold degeneracy is consistent with the dimensions of the irreducible representations of the C_{3v} symmetry group, to which the TGNR geometry belongs. Partial charge density plots provide insight into the spatial distribution of those levels: From the upper panel of Fig. 4.2, we observe that the non-degenerated states (peaks 2 and 3) are mainly spread over the TGNR arms. In contrast, the degenerate states further from the

Fermi energy (peak 4) are located at the corners of the TGNR, while those closer to E_f (peak 1) are concentrated at the corners of the inner triangular hole. In the following, we will show how these electronic states influence the transport properties in the extended system.

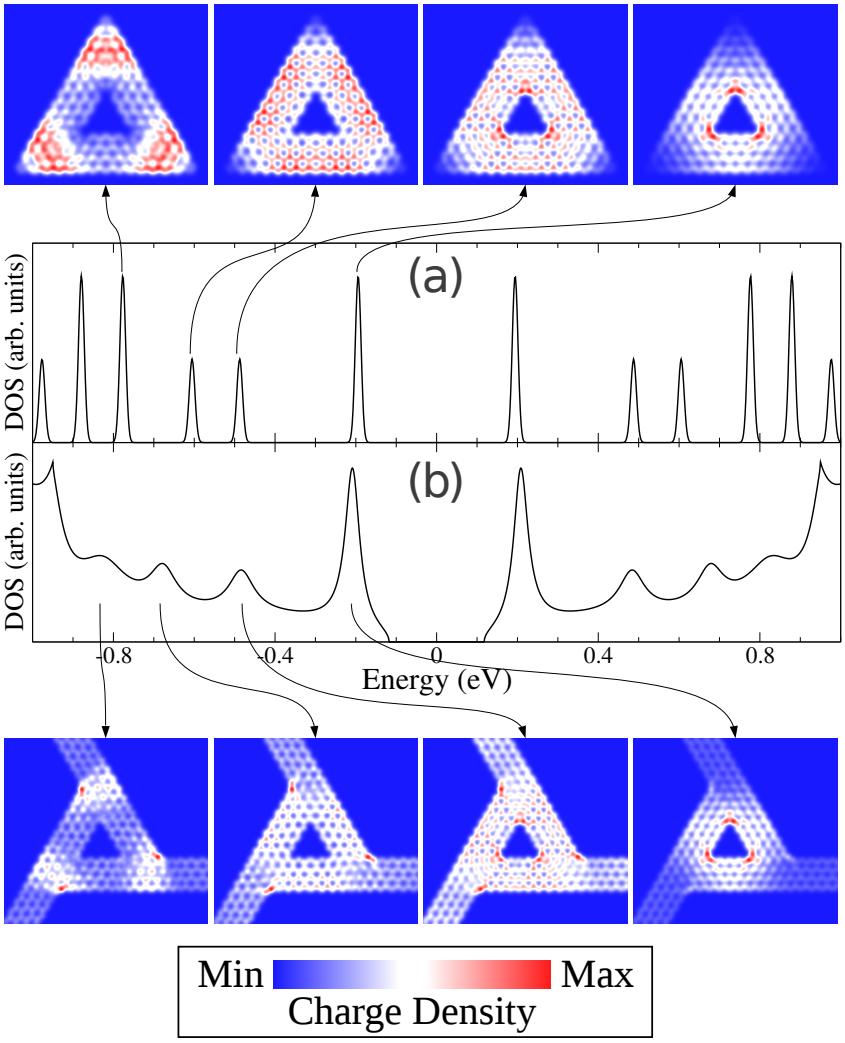

Figure 4.2: Density of states (DOS) for the isolated 11-AGNR based triangle with $N = 30$ (a) and for the corresponding symmetric junction structure (b). Partial charge density plots corresponding to the energy values marked by arrows on the DOS plot of the isolated TGNR and the symmetric junction are provided
on top and bottom of panels (a) and (b) respectively.

In the presence of the 11-AGNR terminals in the symmetric configuration, we note a set of prominent DOS peaks (Fig. 4.2b) that correspond to those of the isolated TGNR, as shown by the partial charge density plots provided in the lower panel of Fig. 4.2. The main difference between the two plots is the significant broadening of the peaks in the extended model, due to coupling to the electrodes and the associated finite lifetime of the electrons in those states. These electronic levels play a central role in the transport properties as revealed by the quantum conductance for the symmetric TGNR junction,

shown in Fig. 4.3a. The TGNR levels behave like resonant states for the transmission, resulting in a set of conductance peaks close to the Fermi energy (all showing a maximal transmission of $\sim 44.5\%$). Note that the conductance is identical for all the paths, since they are geometrically equivalent.

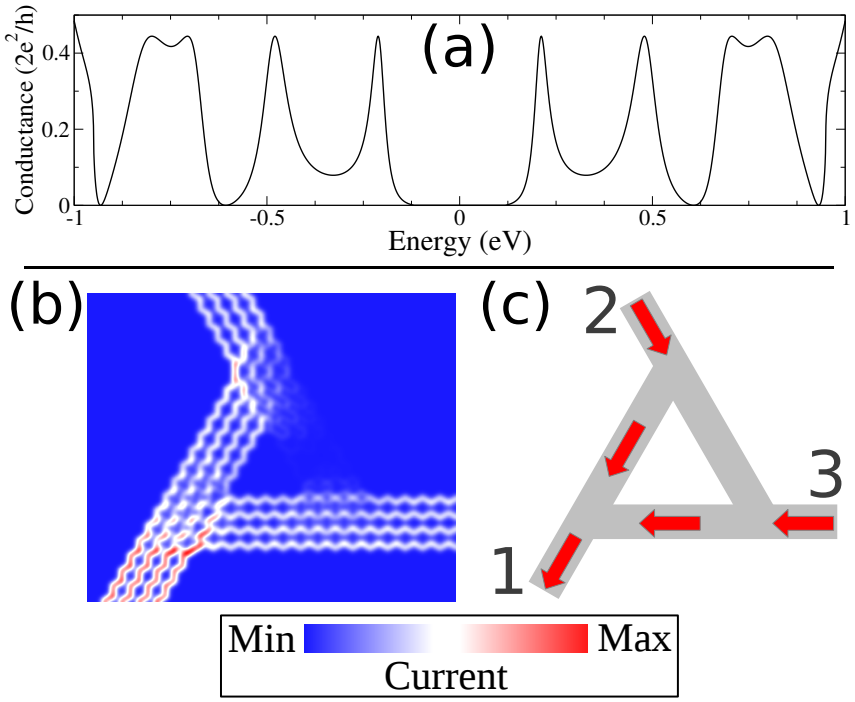

Figure 4.3: (a) Quantum conductance as a function of the energy for the symmetric $N = 30$ junction based on a 11-AGNR. By symmetry, the three possible paths have identical transport curves. (b) Local current profile (with the terminals electronic states filled according to the chemical potentials $\mu_1 = -216$ meV and $\mu_2 = \mu_3 = -206$ meV). (c) Directions for the electronic flow along each arm of the triangle and along each terminal (absent arrows denote places where the local inter-site current does not reach values larger than 10% of the maximal inter-site current in the structure).

We further analyze the transport properties for this symmetric junction with a real space representation of local current profile (Fig. 4.3b) using standard expressions based on lesser and greater Green's functions [39, 15]. Fig 4.3c shows the direction of the current profile only when the inter-site current reaches values larger than 10% of the maximal current flowing between any two sites in the structure. Here the electronic states in the terminals are filled up according to the chemical potentials $\mu_1 = -0.23eV$ and for $\mu_2 = \mu_3 = -0.21eV$. This particular choice was made to include the first conductance peak right below the Fermi energy. One observes that the charge flow is similar in magnitude along terminals 2 (upper side) and 3 (right-hand side), as expected from both the symmetry of the atomic structure and the configuration of the chemical potentials applied to the different terminals. This analysis further confirms the direct influence of the energy levels of the isolated TGNR on electronic transport.

We will now investigate how these properties are affected by changes brought about to details of the TGNR-junction geometry. We will start by considering variations to the atomic structure of the central TGNR, before turning to different strategies to fuse the AGNR terminals. A straightforward way to modify the structure of the central TGNR is to change the size (N) of the AGNR arms composing the triangle. Choosing the $N = 60$ case (using a 11-AGNR) as an example, we observe that for larger TGNR arms, the number of resonant electronic levels close to the Fermi energy increases, as illustrated by the conductance data for this system in the symmetric junction (Fig. 4.4b). This is related to the attenuation of the quantum confinement in the TGNR with larger N, allowing a larger number of electronic states to appear in the same energy interval. Furthermore, varying the width of the AGNR making up the triangular molecule has a different influence on the conductance profile, as the gap for AGNRs is directly related to the ribbon's width. This result can be understood on the basis of the well-established understanding that n-AGNRs can be grouped into families with similar behaviors for the band gap Δ_n as a function of the number n of $C - C$ lines. The families correspond to a different value of index i such that $\Delta_{3i+2} < \Delta_{3i} < \Delta_{3i+1}$, while the gap decreases with increasing n for any of these three sets [14]. The expression of this property is evident in the details of the transport properties of the symmetric TGNR junction, as illustrated by a comparison involving the 5-, 11- and 17-AGNR based structures with $N = 60$. In Fig. 4.4 we show the conductance for the TGNR made of a 5-, 11- and 17-AGNR (whose structures are illustrated in the insets of Fig. 4.4a-c, respectively). We observe that the 5-AGNR and 17-AGNR based systems present larger and smaller gaps, respectively, in comparison to the 11-AGNR case.

In addition to changes to the size of the TGNR node, control over the electronic properties of the three-terminal nanojunction can be achieved by changing the way AGNR terminals are fused into the central junction. To illustrate this point, we considered an alternative way to assemble the junctions by studying the non-symmetric structure depicted in Fig. 4.1c. Such asymmetry promotes significant changes in the transmission profile. Most notably, non-equivalent pathways emerge due to the symmetry breaking between the arms of the junction. This has the effect of enabling the electronic current to flow preferentially through specific paths, giving rise to specific rules to tune the electronic transport in complex GNR-based nanocircuits and yielding network functionalities such as current dividers, etc. For example, Fig. 4.5 depicts the conductance as a function of the energy for the different allowed paths in the non-symmetric junctions based on a 11-AGNR with $N = 30, 60, 90$. For the $N = 30$ case, for instance, one observes that the preferred path (i.e., highest conductance) depends on the energy of the incoming

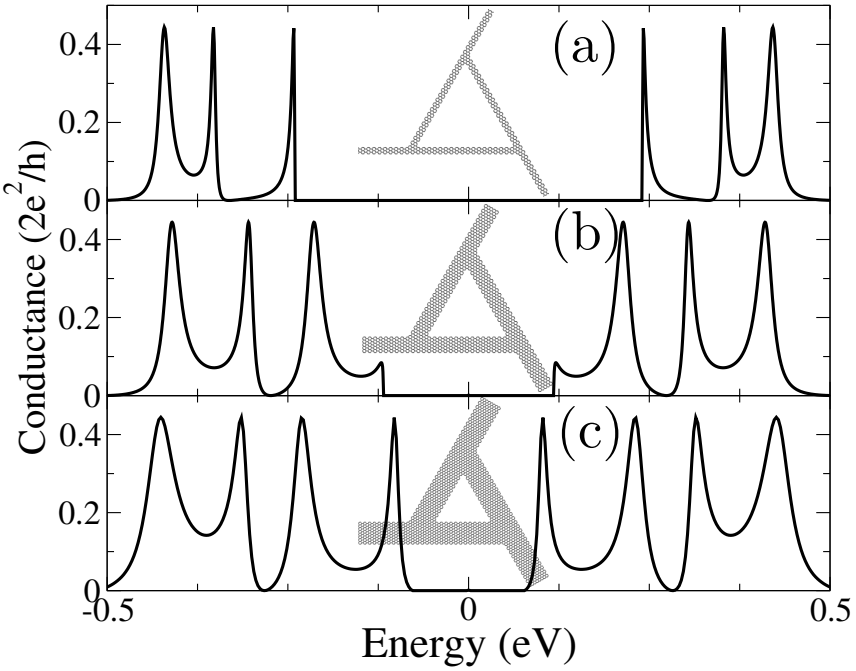

Figure 4.4: Atomic structures of the symmetric TGNR junctions based on the 5- (a), 11- (b) and 17-AGNR (c) with $N = 60$ and the corresponding quantum conductances as a function of the energy (d-e, respectively).

electrons, so that the transmission between terminals 1 and 3 is the largest for energies in the [-0.35 eV, -0.10 eV] interval, while the straight $2 \rightarrow 3$ path is the preferential one for energies within [-0.65 eV, -0.50 eV]. The number of conductance peaks increases within the $[-1\ eV, 0]$ energy range as we increase the size of the central patch (increasing N), in a similar fashion as in the symmetric junction discussed earlier.

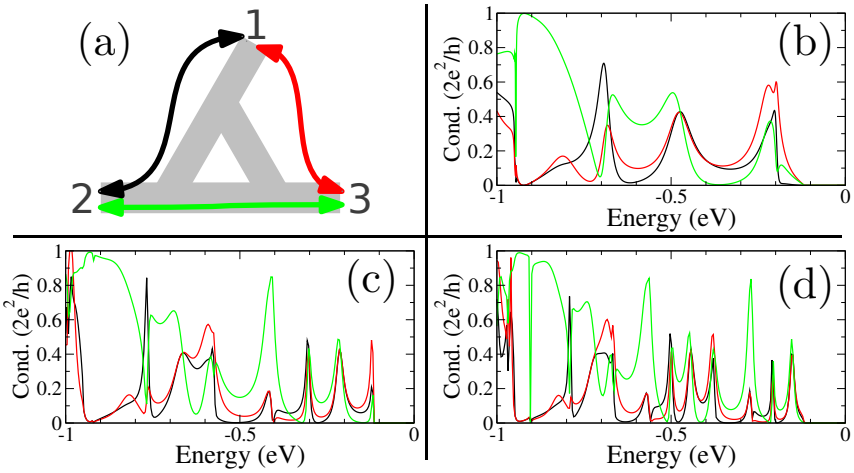

Figure 4.5: (a) Identification for the terminals and the electronic pathways in the non-symmetric junction. (a-d) Quantum conductance as a function of the energy for the different paths in the non-symmetric junction build of a 11-AGNR with $N = 30, 60, 90$, respectively (the curve is symmetric relative to $E_F = 0$ in this tight-binding approach).

Focusing on the $N = 30$ structure, additional features are highlighted by a more thorough analysis of the conductance peaks closest to $E_F = 0$. The plot in Fig. 4.6a, focuses on the peak closest to the Fermi energy and indicates a conductance dip for the $1 \to 3$ and $2 \to 3$ paths and an asymmetric peak for the $1 \to 2$ transmission. We can gain further insight in the transport properties by plotting the local current profiles for different sets of chemical potentials (μ_1, μ_2, μ_3) for terminals 1, 2 and 3, respectively. For all cases we set two of the μ_i $(i = 1, 2, 3)$ to a fixed μ_a value and the other one to a different μ_b chemical potential. We set the numerical values of μ_a and μ_b so as to correspond to the extremes of the energy intervals A and B shown in Fig. 4.6a.

For the interval denoted by A (with $\mu_a = -186$ meV and $\mu_b = -183$ meV), for instance, we have three options to choose how the terminal are filled out-of-equilibrium according to the chemical potential μ_b. Setting μ_b to the first terminal results in the current profile shown in Fig. 4.6b. The positions where the currents are larger than 10% of the maximal inter-site current are shown below the current plot,similar to the representation shown in Fig. 4.3c). This plots shows that the maximal contribution to the current takes place at the corners of the triangular hole. We observe that, as the $1 \to 2$ conductance is suppressed for this interval, the current preferably flows from terminal 1 to terminal 3. Note that the current is most likely to flow through arms 1–2 and 2–3 instead of passing straight through arm 1–3. Setting the terminal 2 to μ_b (Fig. 4.6c), the $2 \to 1$ charge flux is suppressed (as expected from the corresponding conductance value) and the $2 \to 3$ flow follows a non trivial trajectory since it goes through the 1–2 and 1–3 arms instead of going straight through 2–3. In addition, we observe a significant amount of current flowing through the 2–3 arm, but in the opposite direction relative to the net flux between the terminals, thereby creating a circulating current around the TGNR which is larger than the net flux between the terminals.

Moving to interval B, we choose $\mu_a = -206$ meV and $\mu_b = -203$ meV and set terminal 2 to μ_b (Fig. 4.6d). We note that no terminal experiences an inter-site current higher than 10% of the maximal inter-site current in the system. On the other hand, most current is associated to a circulation flow around the triangle. Setting μ_b to terminal 3 (Fig. 4.6e), we observe currents larger than 10% of the maximal value for both terminals 1 and 2 (since both conductance values are nonzero). However, the charge in the 1–3 arm flows preferentially from 1 to 3, in contrast to the net flux between the terminals which is from 3 to 1. The combination of these effects produce a circulating current around the TGNR.

These findings open up potential opportunity for application of these systems for complex electronics but also for chemical sensors and switches, based on local transformations to the triangular graphene patches. The complex rules to control electronic paths in the

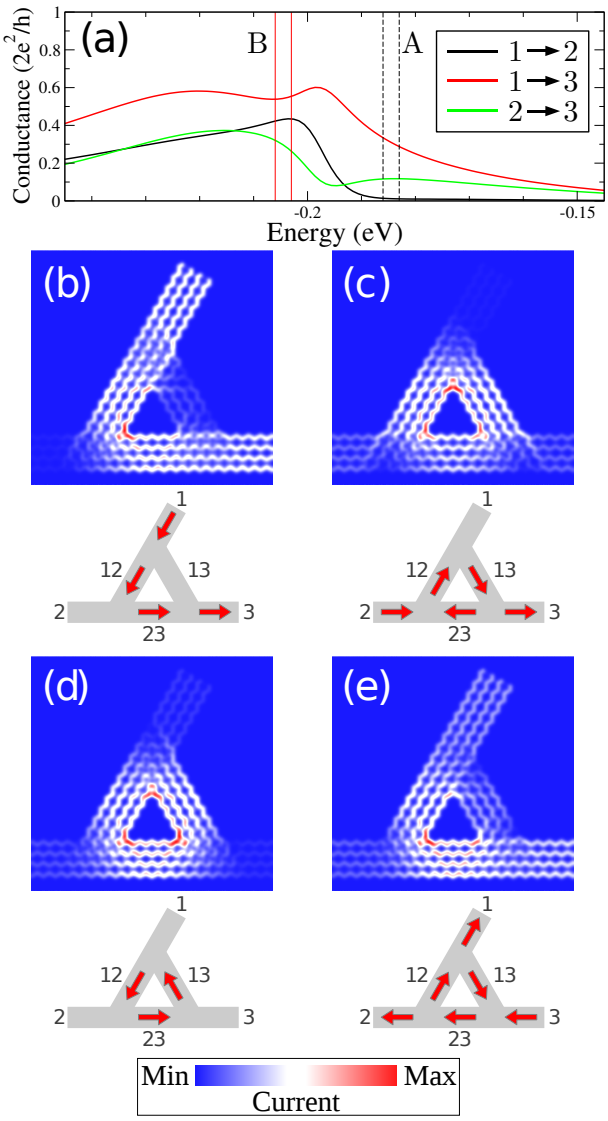

Figure 4.6: (a) Plot showing details of the conductance peak closest to the Fermi energy for the non-symmetric junction built from a 11-AGNR with N=30. The energy intervals A and B that are used to plot the local current profiles in (b-e) are also marked on the figure. The colors (black, red and green) mean the same pathways represented in Fig. 4.5. Local current profiles for the interval A are obtained with $\mu_1 = -183$ meV and $\mu_2 = \mu_3 = -186$ meV (b) and with $\mu_2 = -183$ meV and $\mu_1 = \mu_3 = -186$ meV (c). The local current profiles for the interval B are obtained with $\mu_2 = -203$ meV and $\mu_1 = \mu_3 = -206$ meV (d) and with $\mu_3 = -203$ meV and $\mu_1 = \mu_2 = -206$ meV (e). Along with the plots, we show the direction of the current flow along each arm of the central triangle and along each terminal where the inter-site current reaches values of at least 10% of the maximal inter-site current in the system.

non-symmetric structure, for example, can be used to create prototypes for logical devices based on the non-trivial interplay between bias voltage and the direction of the flow of electrons. In addition, the large, net circulating current is expected to be strongly influenced by the presence of a perpendicular magnetic field, thereby lending support to the development of spintronic properties. While the investigation of such feature is beyond

the scope of the present work, previously published results suggest the use of an external magnetic field to modulate electronic properties in carbon nanotubes [40] and circulating currents in ring-like geometries such as carbon nanotoroids [41]. In fact, investigating the influence not only of external magnetic fields, but also of simple mechanical strain [42] are study perspectives which can revel additional behaviors useful for the development of new nanoscaled devices based on the systems studied here as uniaxial strain can, for instance, break the system's symmetry.

5 Conclusions

We described the transport properties of three-terminal systems composed of triangular-shaped AGNR nanojunctions. We studied how geometric details of the system, such as the atomic structure of the central TGNR and the symmetry of the terminal arrangement, affect the transport behavior. In addition, the selection of specific electronic energies enables the selection of particular pathways for the electrical current across the junction. It was found that this selection is determined by the specific boundary conditions imposed by the triangular shape of the central patch. These results illustrate the fundamental importance of structural geometry for the transport properties and provide guidelines paving the way for the application of such systems in nanoelectronics.

APPENDIX A – Additional Methods

A.0.1 Hartree method

In this approach, a one electron equation is defined as:

$$\hat{H}_{Hartree}\psi_i^\sigma(\mathbf{r}) = -\frac{\hbar^2}{2m_e}\nabla^2\psi_i^\sigma(\mathbf{r}) + V_{Hartree}\psi_i^\sigma(\mathbf{r}) = \mathcal{E}_i^\sigma\psi_i^\sigma(\mathbf{r}), \tag{A.1}$$

where $V_{Hartree}$ is an effective potential that represents the effect of all electron that act on each electron of spin σ. Moreover a different potential is written for each electron to avoid the self-interaction. The ground state is found by occupying the lowest eigenstates obeying the exclusion principle [21].

A.0.2 Hartree-Fock method

This method was first applied to atoms in 1930 by Fock. In this approach the wave-function is antisymmetric and written in a determinant form for a fixed number N of electrons, and this determinant minimizes the total energy. If there is no spin-orbit interaction, the determinant wave-function can be written as a Slater determinant

$$\phi = \frac{1}{\sqrt{N!}}\begin{bmatrix} \phi_1(\mathbf{r}_1,\sigma_1) & \phi_1(\mathbf{r}_2,\sigma_2) & \phi_1(\mathbf{r}_3,\sigma_3) & ... \\ \phi_2(\mathbf{r}_1,\sigma_1) & \phi_2(\mathbf{r}_2,\sigma_2) & \phi_2(\mathbf{r}_3,\sigma_3) & ... \\ \phi_3(\mathbf{r}_1,\sigma_1) & \phi_3(\mathbf{r}_2,\sigma_2) & \phi_3(\mathbf{r}_3,\sigma_3) & ... \\ . & . & . & ... \\ . & . & . & ... \end{bmatrix}. \tag{A.2}$$

The Hartree-Fock approach is to minimize the total energy with respect to all degrees of freedom in the wave-function with the restriction that it has the Slater form A.2. The

expectation value of the Hamiltonian is given by:

$$\begin{aligned}\langle\phi|\hat{H}|\phi\rangle &= \sum_{i,\sigma}\int d\mathbf{r}\psi_i^{\sigma *}(\mathbf{r})\left[-\frac{1}{2}\nabla^2 + V_{ext}(\mathbf{r})\right]\psi_i^{\sigma}(\mathbf{r}) + E_{II} \\ &+ \frac{1}{2}\sum_{i,j,\sigma_i,\sigma_j}\int d\mathbf{r}d\mathbf{r}'\psi_i^{\sigma_i *}(\mathbf{r})\psi_j^{\sigma_j *}(\mathbf{r}')\frac{1}{|\mathbf{r}-\mathbf{r}'|}\psi_i^{\sigma_i}(\mathbf{r})\psi_j^{\sigma_j}(\mathbf{r}') \\ &- \frac{1}{2}\sum_{i,j,\sigma}\int d\mathbf{r}d\mathbf{r}'\psi_i^{\sigma *}(\mathbf{r})\psi_j^{\sigma *}(\mathbf{r}')\frac{1}{|\mathbf{r}-\mathbf{r}'|}\psi_j^{\sigma}(\mathbf{r})\psi_i^{\sigma}(\mathbf{r}'),\end{aligned} \tag{A.3}$$

where we have the Hartree potential and the exchange potential defined as

$$V_{Hartree}(\mathbf{r}) = \frac{e^2}{4\pi\epsilon_0}\sum_{i,\sigma_j}\int d\mathbf{r}'\frac{\psi_j^{\sigma_j *}(\mathbf{r}')\psi_j^{\sigma_j}(\mathbf{r}')}{|\mathbf{r}-\mathbf{r}'|}, \tag{A.4}$$

$$V_{exchange}(\mathbf{r}) = -\frac{e^2}{4\pi\epsilon_0}\sum_{j}\int d\mathbf{r}'\frac{\psi_j^{\sigma *}(\mathbf{r}')\psi_i^{\sigma}(\mathbf{r}')}{|\mathbf{r}-\mathbf{r}'|}\frac{\psi_j^{\sigma}(\mathbf{r})}{\psi_i^{\sigma}(\mathbf{r})}. \tag{A.5}$$

The presence of the exchange potential is the main difference between Hartree and Hartree-Fock approaches. This potential does not have a classical analogous, so it is difficult understanding its physical meaning. The exchange term represents two effects: Pauli exclusion and the self-term that must be subtracted to cancel the spurious self-interaction included in the direct Coulomb Hartree energy. As the exchange term is negative, its effect is always to lower the energy that can be viewed as the interaction of each electron with a fictitious positive charge that we called "exchange hole".

A.0.3 Density Functional Theory (DFT)

If we consider a system of N electrons in a stationary state that would obey the stationary Schrödinger equation:

$$\left[-\frac{\hbar^2}{2m}\sum_i \nabla_i^2 + \frac{1}{2}\sum_{i\neq j} v(\mathbf{r}_i,\mathbf{r}_j)\right]\Psi(\mathbf{r}_1,...,\mathbf{r}_n) = E_i\Psi(\mathbf{r}_1,...,\mathbf{r}_n), \tag{A.6}$$

we would try to avoid the complication of searching for the many-electron wavefunction $\psi(\mathbf{r}_1,...,\mathbf{r}_n)$, concentrating on an electron density $n(\mathbf{r})$ instead. The electron density is a physical observable, it can be measured, calculated and easily visualized and contains all the information in the many-body wave-functions for the ground state and all excited states.

DFT, different from Hartree and HF, is not a approximation, it is an exact theory. In this theory, any property of a system of many interacting particles can be viewed as a functional of the ground state density $n_0(\mathbf{r})$. The original density functional theory of

quantum systems was proposed by Thomas and Fermi in 1927. This approximation is not accurate enough to electronic structure calculations, but it illustrates the way DFT works. On the other hand, Hohenberg and kohn [43] formulated DFT as an exact theory of many-body systems in 1964. Density functional theory is based upon two theorems first proved by these authors.

1^{st} Theorem: If any system of interacting electrons is under the influence of an external potential $V_{ext}(\mathbf{r})$, this potential is determined uniquely (except by a constant) by the electronic density of the ground state $n_0(\mathbf{r})$.

2^{st} Theorem: If a universal functional for the energy $E[n]$ is terms of the density $n(\mathbf{r})$ can be defined for any external potential, so this functional has its global minimum (ground state energy) for the exact density $n_0(\mathbf{r})$ corresponding to the ground state.

The energy functional is written as,

$$E_{HK}[n] = T[n] + E_{electronic}[n] + \int d(\mathbf{r}) V_{ext}(\mathbf{r}) n(\mathbf{r}), \tag{A.7}$$

where T is the kinetic energy functional, V_{ext} is the external potential including the nuclei contribution and $E_{electronic}$ accounts for all the electron-electron interactions.

In this dissertation we use tight-binding that is a simpler model to describe the elements of Hamiltonian in our electronic structure calculations. So we give more attention and discuss with more details this model in next sections.

A.1 LCAO

We need a basis-set to expand the wavefunctions and solve the Schrödinger equation. An appropriate choice for these basis functions is a set of atomic-like functions centered on the atom sites that are called Linear Combination of Atomic Orbitals (LCAO) method [21]. On each site the basis functions can be written as radial functions multiplied by spherical harmonics,

$$\chi_{nlm}(\mathbf{r}) = \chi_{nl}(r) Y_{lm}(\hat{\mathbf{r}}), \tag{A.8}$$

orbitals with $m = 0$ are real, but when $m \neq 0$ we can define a real basis functions using the real angular functions:

$$Y_l^{\pm} m = \frac{1}{2}(Y_{lm} \pm Y_{lm}^*). \tag{A.9}$$

To illustrate this method, we apply it to solve a simple problem that is a benzene molecule. This molecule is composed of a six identical atoms which form a regular hexagon. We consider only the π orbital and consider an electron which can be localized

on each atom. Each wavefunction is expressed as a sum of those sites:

$$\phi_i(r) = \sum_{\mu=1}^{6} c_{i\mu}\chi_\mu(\mathbf{r}). \tag{A.10}$$

The Hamiltionian is a 6x6 matrix, where the diagonal elements is identical and equal to ϵ, in other words $H_{ij} = \epsilon$ when $i = j$. The nearest-neighbor pair is identical, so each nearest-neighbor element is identical and we called γ, then $H_{ij} = -\gamma$ when $i \neq j$ with i and j being first-neighbors. In this model, known as the Hückel approach, it is assumed that atoms further away than nearest-neighbor positions do not contribute to this electron sharing. Diagonalizing the matrix Hamiltonian below, we find the six eigenvalues and their respective eigenvectors.

$$\begin{bmatrix} -\epsilon & -\gamma & 0 & 0 & 0 & -\gamma \\ -\gamma & -\epsilon & -\gamma & 0 & 0 & 0 \\ 0 & -\gamma & -\epsilon & -\gamma & 0 & 0 \\ 0 & 0 & -\gamma & -\epsilon & -\gamma & 0 \\ 0 & 0 & 0 & -\gamma & -\epsilon & -\gamma \\ -\gamma & 0 & 0 & 0 & -\gamma & -\epsilon \end{bmatrix}. \tag{A.11}$$

The six eigenvalues are $\epsilon - 2\gamma$, $\epsilon - \gamma$, $\epsilon - \gamma$, $\epsilon + \gamma$, $\epsilon + \gamma$, $\epsilon + 2\gamma$. The eigenvectors are:

$$\begin{aligned} |\phi_1\rangle &= \frac{1}{\sqrt{6}}(|1\rangle + |2\rangle + |3\rangle + |4\rangle + |5\rangle + |6\rangle) \\ |\phi_2\rangle &= \frac{1}{2}(|1\rangle + |6\rangle - |3\rangle - |4\rangle) \\ |\phi_3\rangle &= \frac{1}{2}(|4\rangle + |5\rangle - |1\rangle - |2\rangle) \\ |\phi_4\rangle &= \frac{1}{2}(|1\rangle - |6\rangle - |3\rangle + |4\rangle) \\ |\phi_5\rangle &= \frac{1}{2}(|4\rangle - |5\rangle + |1\rangle - |2\rangle) \\ |\phi_6\rangle &= \frac{1}{\sqrt{6}}(|1\rangle - |2\rangle + |3\rangle - |4\rangle + |5\rangle - |6\rangle). \end{aligned} \tag{A.12}$$

APPENDIX B – Publications

B.1 Publication related to this dissertation

- A. L. Mariano Torres Costa, V. Meunier, E. C. Girao. "Electronic transport in three-terminal triangular carbon nanopatches". Nanotechnology **25**(4) (2014).

B.2 Publication not related to this dissertation

- M. D. S. Price, E. Cruz-Silva, A. L. M. T. Costa, F. M. Vasconcelos, E. C. Girão, S. B. Zhang, V. Meunier. "Electronic and transport properties of graphene nanoribbon barbell-shaped heterojunctions". Physica Status Solidi (B) **250**(11) (2013).

References

[1] D. V. Kosynkin, A. L. Higginbotham, A. Sinitskii, J. R. Lomeda, A. Dimiev, B. K. Price, J. M. Tour. "Longitudinal unzipping of carbon nanotubes to form graphene nanoribbons". *Nature* **458**(7240), 872 (2009).

[2] J. Cai, P. Ruffieux, R. Jaafar, M. Bieri, T. Braun, S. Blankenburg, M. Muoth, A. P. Seitsonen, M. Saleh, X. Feng, K. Muellen, R. Fasel. "Atomically precise bottom-up fabrication of graphene nanoribbons". *Nature* **466**(7305), 470 (2010).

[3] R. P. Feynman. *There's Plenty of Room at the Bottom.* American Physical Society meeting at Caltech.

[4] E. C. Girão, Y. Liebold-Ribeiro, J. A. Batista, E. B. Barros, S. B. Fagan, J. Mendes Filho, M. S. Dresselhaus, A. G. Souza Filho. "Functionalization of single-wall carbon nanotubes through chloroform adsorption: theory and experiment". *Physical Chemistry Chemical Physics* **12**(7), 1518 (2010).

[5] S. J. Tans, A. R. M. Verschueren, C. Dekker. "Room-temperature transistor based on a single carbon nanotube". *Nature* **393**(6680), 49 (1998).

[6] M. M. Shulaker, G. Hills, N. Patil, H. Wei, H.-Y. Chen, H.-S. P. Wong, S. Mitra. "Carbon nanotube computer". *Nature* **501**(7468), 526 (2013).

[7] R. Saito, G. Dresselhaus, M. S. Dresselhaus. *Physical Properties of Carbon Nanotubes.* London: Imperial College Press.

[8] H. W. Kroto, J. R. Heath, S. C. Obrien, R. F. Curl, R. E. Smalley. "C-60 - Buckminsterfullerene". *Nature* **318**(6042), 162 (1985).

[9] S. Iijima. "Helical microtubules of graphitic carbon". *Nature* **354**(6348), 56 (1991).

[10] S. Iijima, T. Ichihashi. "Single-shell carbon nanotubes of 1 nm diameter". *Nature* **363**(6430), 603 (1993).

[11] D. S. Bethune, C. H. Kiang, M. S. Devries, G. Gorman, R. Savoy, J. Vazquez, R. Beyers. "Cobalt-catalyzed growth of carbon nanotubes with single-atomic layerwalls". *Nature* **363**(6430), 605 (1993).

[12] K. Novoselov, A. Geim, S. Morozov, D. Jiang, Y. Zhang, S. Dubonos, I. Grigorieva, A. Firsov. "Electric field effect in atomically thin carbon films". *Science* **306**(5696), 666 (2004).

[13] R. Van Noorden. "The trials of new carbon". *Nature* **469**(7328), 14 (2011).

[14] Y.-W. Son, M. L. Cohen, S. G. Louie. "Energy gaps in graphene nanoribbons". *Physical Review Letters* **97**(21), 216803 (2006).

[15] E. C. Girão, E. Cruz-Silva, V. Meunier. "Electronic transport properties of assembled carbon nanoribbons". *ACS Nano* **6**(7), 6483 (2012).

[16] L. Pisani, J. A. Chan, B. Montanari, N. M. Harrison. "Electronic structure and magnetic properties of graphitic ribbons". *Physical Review B* **75**(6), 064418 (2007).

[17] D. Gunlycke, C. T. White. "Tight-binding energy dispersions of armchair-edge graphene nanostrips". *Physical Review B* **77**, 115116 (2008).

[18] Y.-W. Son, M. L. Cohen, S. G. Louie. "Half-metallic graphene nanoribbons". *Nature* **444**(7117), 347 (2006).

[19] X. Wang, H. Dai. "Etching and narrowing of graphene from the edges". *Nature Chemistry* **2**(8), 661 (2010).

[20] V. V. Mitin, D. I. Sementsov, N. Z. Vagidov. *Quantum mechanics for nanostructures.* Cambridge University Press.

[21] R. M. Martin. *Electronic structure: Basic Theory and Practical Methods.* Cambridge University Press: Cambridge, UK.

[22] N. W. Ashcroft, N. D. Mermin. *Solid state Physics.* Thomson Learning, Inc.

[23] F. Bloch. *Zeitschrift fur Physik* **52**, 555 (1928).

[24] O. V. Yazyev. "Emergence of magnetism in graphene materials and nanostructures". *Reports on Progress in Physics* **73**(5), 056501 (2010).

[25] E. C. Girão, L. Liang, E. Cruz-Silva, A. G. Souza Filho, V. Meunier. "Emergence of atypical properties in assembled graphene nanoribbons". *Physical Review Letters* **107**, 135501 (2011).

[26] E. Costa Girão, E. Cruz-Silva, L. Liang, A. G. S. Filho, V. Meunier. "Structural and electronic properties of graphitic nanowiggles". *Physical Review B* **85**, 235431 (2012).

[27] R. Landauer. "Electrical resistance of disordered one-dimensional lattices". *Philosophical Magazine* **21**(172), 863 (1970).

[28] R. Landauer. "Conductance determined by transmission - probes and quantized constriction resistance". *Journal of Physics-Condensed Matter* **1**(43), 8099 (1989).

[29] S. Datta. *Quantum Transport: Atom to Transistor.* Cambridge University Press (2005).

[30] M. Di Ventra. *Electrical Transport in Nanoscale Systems.* Cambridge University Press (2008).

[31] A. L. Mariano Torres Costa, V. Meunier, E. C. Girao. "Electronic transport in three-terminal triangular carbon nanopatches". *Nanotechnology* **25**(4) (2014).

[32] M. Bieri, M.-T. Nguyen, O. Groening, J. Cai, M. Treier, K. Ait-Mansour, P. Ruffieux, C. A. Pignedoli, D. Passerone, M. Kastler, K. Muellen, R. Fasel. "Two-Dimensional Polymer Formation on Surfaces: Insight into the Roles of Precursor Mobility and Reactivity". *Journal of the American Chemical Society* **132**(46), 16669 (2010).

[33] L. Grill, M. Dyer, L. Lafferentz, M. Persson, M. V. Peters, S. Hecht. "Nano-architectures by covalent assembly of molecular building blocks". *Nature Nanotechnology* **2**(11), 687 (2007).

[34] J. Lu, P. S. E. Yeo, C. K. Gan, P. Wu, K. P. Loh. "Transforming C(60) molecules into graphene quantum dots". *Nature Nanotechnology* **6**(4), 247 (2011).

[35] L. Lafferentz, F. Ample, H. Yu, S. Hecht, C. Joachim, L. Grill. "Conductance of a Single Conjugated Polymer as a Continuous Function of Its Length". *Science* **323**(5918), 1193 (2009).

[36] C.-A. Palma, P. Samori. "Blueprinting macromolecular electronics". *Nature Chemistry* **3**(6), 431 (2011).

[37] A. V. Talyzin, I. V. Anoshkin, A. V. Krasheninnikov, R. M. Nieminen, A. G. Nasibulin, H. Jiang, E. I. Kauppinen. "Synthesis of graphene nanoribbons encapsulated in single-walled carbon nanotubes". *Nano Letters* **11**(10), 4352 (2011).

[38] M. Fujihara, Y. Miyata, R. Kitaura, Y. Nishimura, C. Camacho, S. Irle, Y. Iizumi, T. Okazaki, H. Shinohara. "Dimerization-initiated preferential formation of coronene-based graphene nanoribbons in carbon nanotubes". *The Journal of Physical Chemistry C* **116**(28), 15141 (2012).

[39] K. Kazymyrenko, X. Waintal. "Knitting algorithm for calculating Green functions in quantum systems". *Physical Review B* **77**(11), 115119 (2008).

[40] S. Roche, R. Saito. "Effects of magnetic field and disorder on the electronic properties of carbon nanotubes". *Physical Review B* **59**, 5242 (1999).

[41] L. Liu, G. Y. Guo, C. S. Jayanthi, S. Y. Wu. "Colossal paramagnetic moments in metallic carbon nanotori". *Physical Review Letters* **88**(21), 217206 (2002).

[42] S. H. R. Sena, J. M. P. Jr, G. A. Farias, F. M. Peeters, R. N. C. Filho. "The electronic properties of graphene and graphene ribbons under simple shear strain". *Journal of Physics: Condensed Matter* **24**(37), 375301 (2012).

[43] P. Hohenberg, W. Kohn. "Inhomogeneous Electron Gas". *Physical Review B* **136**(3B), B864 (1964).